Graduate School Form 30
Updated 1/15/2015

PURDUE UNIVERSITY
GRADUATE SCHOOL
Thesis/Dissertation Acceptance

This is to certify that the thesis/dissertation prepared

By Kylie A. Corry

Entitled
Novel Insights into the Mechanistic Gene Regulation of STAT3 in Bone Cells

For the degree of Master of Science

Is approved by the final examining committee:

Dr. Jiliang Li
Chair

Dr. Joseph Bidwell

Dr. Sungsoo Na

To the best of my knowledge and as understood by the student in the Thesis/Dissertation Agreement, Publication Delay, and Certification Disclaimer (Graduate School Form 32), this thesis/dissertation adheres to the provisions of Purdue University's "Policy of Integrity in Research" and the use of copyright material.

Approved by Major Professor(s): Dr. Jiliang Li

Approved by: Dr. Simon Atkinson 6/25/2015
Head of the Departmental Graduate Program Date

NOVEL INSIGHTS INTO THE MECHANISTIC GENE REGULATION OF STAT3 IN BONE CELLS

A Thesis
Submitted to the Faculty
of
Purdue University
by
Kylie A. Corry

In Partial Fulfillment of the
Requirements for the Degree
of
Master of Science

August 2015
Purdue University
Indianapolis, Indiana

To my parents,

You still owe me a tree house.

ACKNOWLEDGEMENTS

I would firstly like to thank my advisor Dr. Jiliang Li for his patience and mentorship over the past two years. I would also like to thank Dr. Joseph Bidwell and Dr. Sungsoo Na for serving on my thesis committee. For assistance with histology work, I give my thanks to Yongqi Yu. For maintaining the cell line, I would like to thank Pei Zhang. For running the biomechanical testing, I would like to thank Alycia Berman and the rest of the Dr. Joseph Wallace lab. Lastly, I would like to express my appreciation to all current and past members of the Li lab for their guidance, friendship, and support in completing my thesis work.

TABLE OF CONTENTS

LIST OF TABLES

LIST OF FIGURES

ABSTRACT

Corry, Kylie A. M.S., Purdue University, August 2015. Novel Insights into the Mechanistic Gene Regulation of STAT3 in Bone Cells. Major Professor: Jiliang Li.

Many cells are involved in the orchestra that is bone homeostasis--particularly osteoclasts and osteoblasts, which mediate remodeling of bones. This creates a balance that must be kept in check, otherwise pathologies arise. The JAK-STAT signaling pathway is crucial to maintaining this balance. It has long been known that the transcription factor STAT3 has more profound effects on bone homeostasis than other members of the STAT family of proteins. Recently, a genetic condition called Job's Syndrome has been specifically linked to point mutations in the *Stat3* gene. These patients present with severe bone abnormalities, including prominent foreheads, broad nasal bridges, and abnormal eye spacing. For this reason, our lab has extensively studied conditional knockouts of *Stat3* in all three types of bones cells in mice and observed severe deficiencies in numerous parameters of normal bone phenotypes. STAT3 seems to play a principal role in the signaling that takes place upon mechanical loading of bone tissues and calling cells into action where they are needed. Furthermore, STAT3 has been found to be up-regulated in the early-response gene cluster following mechanical loading.

Our current approach to studying STAT3's effects on bone includes both *in vivo* and *in vitro* comparisons of WT and KO STAT3 models. The conditional knock-out of STAT3 in 8-week old mice revealed significant phenotypic variations as compared to the WT controls, while no significant differences were observed in cKO newborn pups. We also looked at immortalized WT and STAT3 KO cell lines. The STAT3 KO cells had diminished proliferation rates and decreased differentiation capabilities. Furthermore, STAT3 KO cells showed significantly reduced mRNA levels of both Wnt3a and Wnt5a when exposed to fluid shear stress.

By employing available ChIP-seq data, we were able to elucidate the genome-wide binding patterns of STAT3. From the peak distribution, we can begin to uncover novel downstream effectors of STAT3 signaling that are responsible for the observed phenotypes in our conditional knockout mouse model. A preliminary look at the ChIP-seq data reveals Wnt and Nrf2 signaling to be under the putative control of STAT3. In our further research, we endeavor to experimentally confirm the ChIP-seq data for STAT3 with RNA-seq experiments in the hopes of finding potential therapeutic targets for bone pathologies.

CHAPTER 1. INTRODUCTION

1.1 Skeletal System Biology

The formation of the skeletal system is the distinguishing factor between vertebrates and invertebrates. The skeleton is much more than a mere framework for our bodies. The structure and conformation of the 206 bones that comprise the human skeleton establishes the foundation for our physical appearance; its differentiation and growth during embryonic development determines our size at birth, while its deterioration in later life marks the downward spiral away from the rapidity and dexterity of youth. Much focus is put on the mechanical aspects of bone, where it functions to transmit the forces generated by the muscles and creates a protective barrier to the vital organs. However, bone also provides storage for the body's supply of calcium and phosphorus. Bone has also been categorized as an endocrine organ for its role in balancing phosphate and energy metabolism through its secretion of two hormones, fibroblast growth factor 23 (FGF-23) and osteocalcin (1).

1.2 Skeletal Anatomy

The skeleton can be divided into several groups: long bones, short bones, flat bones, irregular bones, and sesmoid bones. Long bone anatomy can further be divided into the ephiphysis, metaphysis, and diaphysis. The epiphyses are found at either end of the long bone, proximally and distally. They are the portion of the bone that articulates with the neighboring bones and are therefore covered with articular cartilage. The metaphysis is a wide, intermediate region between the epiphysis and the diaphysis that is considered part of the growth plate, or growing region. The diaphysis, or midshaft, of a long bone is the elongated, hollow portion between the metaphyses that surrounds a central marrow cavity that contains the bone marrow (2). The skeleton is divided into the axial and appendicular portions. The axial skeleton is comprised of the bones that form the axis of the body and the bones that support and protect the organs of the head and trunk regions, including the bones of the skull, vertebral column, and rib cage. The appendicular skeleton is comprised of the bones of the pelvic and pectoral girdles as well as the bones of the upper and lower extremities. The girdles provide a point of attachment to the axial skeleton.

1.3 Bone Tissue Structure

Two types of bone tissue exist: compact and spongy bone. These types are distinguished not only by their porosity level, but also by where they are found and their functions. Compact, or cortical, bone is relatively solid and can be found where external stresses come from a limited range of directions. Spongy, or cancellous, bone is less compact and is made of a network of bony rods, called trabeculae, which are separated by spaces. Spongy bone comprises the epiphyses of long bones and can withstand stresses from many directions. The trabeculae work by dissipating the external forces to the stronger, more massive cortical bone (1).

The outer surface of all bones is covered in a fibrous tissue called the periosteum. The fibers of tendons and ligaments intertwine with those of the periosteum to form a stable bridge between bones and muscles or one bone to another. The periosteum serves many purposes for bone, including isolating it from surrounding tissues, providing a route for nervous and circulatory supplies, and aiding in the growth and repair of bone. Lining the inside of bone is the endosteum. The functions of the endosteum are similar to those of the periosteum. Both types of bone tissue are composed of functional units called osteons. In compact bone, the osteons are arranged into Haversian systems. Concentric circles of lamellae are formed around central canals and run parallel to the long axis of the bone and contain spaces called lacunae where mature bone cells are found. Canaliculi are small channels that connect lacunae and link them to nearby blood vessels. In spongy bone, however, half osteons, or hemiosteons, instead of lamellae, form the trabecular pieces.

Because of their proximity to the marrow cavity, the hemiosteons do not require central canals to supply their nutrients (1).

Bone is a composite structure arranged in a hierarchical manner, whose extracellular matrix is composed of mineral, collagen, water, noncollagenous proteins, and lipids. The mineral portion of bone makes up between 50-70% of the adult bone and is composed of hyroxyapatatite crystals [$Ca_{10}(PO_4)_6(OH)_2$]. The majority of the collagen in bone is cross-linked type 1 collagen, and it accounts for 20-25% of its composition. About 10% of the collagens in bone are types III and V. The amount and maturity level of type 1 collagen found in bone has a profound effect on bone strength and energy required to fracture. The mineral portion of bone provides stiffness while the collagen portion of bone provides resilience and ductility (1).

1.4 Bone Cells

Osteocytes are mature bone cells and are also the most abundant cells in bone. They work to maintain the normal bone structure by recycling the excess calcium in the bony matrix and by assisting in repairs. Osteocytes are also thought to be the main bone cells that sense mechanical loads and transduce the signals to induce a biomechanical response. This process is mediated through their intricate network of cellular extensions, providing connections to neighboring osteocytes via gap junctions (3). Osteoclasts, the bone resorbing cells, are very large and contain 50 or more nuclei. They are derived from hematopoietic mononuclear precursor cells. Osteoclasts secrete acids and enzymes that function to dissolve bone matrix thereby releasing stored minerals. This process helps to regulate the levels of calcium and phosphate in the body. Osteoblasts, the bone forming cells, deposit calcium salts into the organic matrix of bone. When an osteoblast becomes completely encased in the matrix that it deposited, it begins differentiating into an osteocyte. All of the bone cells are able to communicate with one another either by direct cell contact or indirectly through signaling molecules (4).

1.5 Osteoblasts and Bone Progenitors

Osteoblast cells are derived from mesenchymal progenitors (mesenchymal stem cells). In addition to osteoblasts, these pluripotent progenitor cells are capable of aare involved in the differentiation of osteoblasts, including Hedgehogs, BMPs, TGF-β, PTH, and the Wnts. An important step in the differentiation of osteoblasts is the activation of the transcription factor Runx2. Runx2 is the ‘master switch’ for osteoblast differentiation. This is demonstrated by that fact that mice deficient in Runx2 expression have no mature osteoblasts and fail to form a mineralized matrix (5). The differentiation of the osteoblasts is arrested during both endochondral and intramembranous bone formation. Runx2 goes on to regulate the expression of the zinc-finger-containing transcription factor Osterix (Osx). Mice that lack Runx2 expression also lack expression of Osx, however, Osx-null mice still express Runx2, meaning Osx operates downstream of Runx2. Osx is also required for the complete differentiation of osteoblasts but does not seem to have an effect on the patterning of the skeleton during development as, evidenced by Osx null embryos being indistinguishable from their wild type counterparts (6). Osterix controls the expression of target genes, including osteocalcin, osteopontin, osteonectin, and type I collagen (4,7).

Wnt signaling is also known to heavily influence the generation and survival of osteoblasts. Wnt signaling is especially important in regulating the balance between adipogenesis and osteoblastogenesis—it inhibits adipogenesis and stimulates osteoblastogenesis (8). Conditional knockout of β-catenin, the Wnt intercellular signaling molecule, led the common osteochondroprogenitor cells to exclusively differentiate into chondrocytes rather than osteoblasts during intramembranous and endochondral bone formation (9). Gain-of-function mutations in the co-receptor for Wnt signaling, LRP5, lead to a high bone mass in mice and humans (10). Wnts are also capable of pushing undifferentiated mesenchymal cells towards the osteoblastic phenotype.

1.6 Osteoclast-Osteoblast Communication

In order for bone homeostasis to maintain normal bone mass, the bone cells must communicate with each other. They accomplish this by utilizing cell-to-cell contacts, diffusible paracrine factors, and cell-to-matrix interactions. These processes will ultimately trigger intercellular signaling that modulates bone resorption and formation. The RANKL-RANK-OPG signaling system is one way to control osteoclast formation and, in turn, bone resorption. Stromal cells, osteoblasts, and osteoclasts contain RANKL on their cell surface; however, RANKL can also function in a soluble form. RANKL can bind to two different receptors, RANK or osteoprotegrin/tumor necrosis factor receptor superfamily member 11B (OPG). Osteoclasts precursor cells express RANK as a transmembrane protein receptor while OPG is produced as a soluble, secreted molecule. OPG contains a similar N-terminal region that allows it to function as a decoy receptor for RANKL. When RANKL binds to RANK, it leads to the activation of specific transcription factors that, in turn, will push the differentiation of mononuclear precursor cells into multinucleated osteoclasts. RANKL serves not only to differentiate osteoclasts, but also to promote their survival. OPG protects bone from over-resorption by neutralizing the activity of RANKL. The ratio of RANKL to OPG serves as a determinant of the amount of bone resorption taking place (11,12). Mice deficient in RANK have profound osteopetrosis resulting from a lack of osteoclast differentiation and subsequently decreased bone resorption (13). Though osteoblast-mediated RANKL production was thought to be the main contributor to osteoclast activation, emerging evidence suggests that RANKL produced by osteocytes is just as, if not more, crucial to osteoclast activation (14).

Bidirectional signaling between osteoclasts and osteoblasts also contributes to bone homeostasis. This signaling is mediated by a subgroup of ephrin proteins and their receptors. The ephrin-B-EphB system plays an especially important role in bone homeostasis and has been extensively studied in the context of bone. The bidirectional nature of this type of signaling allows it to couple bone resorption to bone formation. Reverse signaling involves ephrin-B2, expressed on the surface of osteoclasts, binding to Eph-B4 on osteoblasts—inhibiting bone resorption by deactivating hematopoietic precursors. The forward signaling event, from Eph-B4 back to ephrin-B2 on osteoclasts, triggers bone formation by up-regulating osteoblasts specific transcription factors (4,11,12).

1.7 Bone Formation

Mesenchymal stem cells, the precursors to bone cell, found in different regions of the developing embryo are descendants of different cell lineages, therefore, the location of each skeletal formation event will determine from which mesenchymal lineage the new bone is derived. Positional identity of the new bone is acquired early in development, even before the mesenchyme begins to condense. Bone always arises secondary to a preexisting supportive tissue. The formation of bone begins around the third month of fetal development and continues through late adolescence before it begins to decline. Bone can be formed through two distinctly different processes: endochondral or intramembranous ossification.

These types of bone formation differ in the local environment in which they are initiated and in what cells are producing the matrix. Endochondral ossification first begins with the deposition of a hyaline cartilage model by chondrocytes, which later becomes calcified by osteoprogenitor cells. Intramembranous ossification is not preceded by the formation of a cartilaginous template. Mesenchymal stem cells, rather, form condensations and begin differentiating into osteoprogenitor cells that will later become osteoblasts. The majority of bones form through endochondral ossification during development, with the flat bones of the skull, the mandible, and the clavicles being the exceptions. Although intramembranous ossification is often associated only with embryonic development, it is also essential to the natural process of healing bone (15).

1.8 Bone Modeling and Remodeling

The functioning of the osteoclasts and osteoblasts continues even after the epiphyseal plates have closed. Under normal physiological conditions, the activity of the osteoclasts is balanced with that of the osteoblasts during the turnover of bone in a process called bone remodeling. The turnover rate for bone is fairly high, though not every part of bone is affected. This high turnover rate gives bone the ability to respond and adapt to new stresses, mainly in the form of external forces, and is a unique feature among the other connective tissues. Bone remodeling is controlled through local, endocrine, and neuronal factors.

During growth, the rate of bone remodeling is high, with formation exceeding resorption resulting in a net increase in bone mass. This begins to decline later in life when resorption begins to outpace formation.

Bone modeling can be thought of as the uncoupling of bone remodeling, either the formation of bone through osteoblasts or the resorption of bone through osteoclasts, on any given surface, signaled by local tissue strain. Bone modeling is necessary because longitudinal growth alone would not produce the correct geometry. The process of bone modeling allows bone to increase its mass and either maintain or alter its shape. Although the resorption and formation are uncoupled in bone modeling, they must still be coordinated throughout the body to shape the bone. Bone modeling occurs in two phases: an activation phase where precursor cells are recruited to a particular site, and then either formation or resorption of bone. This process will continue until enough bone mass has been added or removed in order to equilibrate the amount of local strains. Bone modeling is less common in the adult under normal physiologic conditions, but some modeling does take place (15).

1.9 Bone Biomechanics

During every day normal activities, bone is called upon to handle dynamic mechanical stimuli. Bone’s ability to deal with these types of stimuli are dependent upon the type of load applied and with what force, as well as the underlying structural properties of the bone receiving the load. Failure occurs if the load exceeds the structural strength of the bone. It is these mechanical demands that heavily influence the biologic response that bone initiates. There are many different types of stresses that bone can incur, including tension, compression, shear, torsion, and bending. When a force is applied to bone in one of these manners, deformation of the bone will take place. The amount of deformation can be graphed as a function as the force applied, producing a force-displacement curve. Extrinsic properties of the bone structure as a whole can be determined from this curve. The initial portion of the curve is linear and is referred to as the elastic region. Within this region of the curve, no energy is lost and no permanent deformation takes place. The slope of the curve in the elastic region is equivalent to the structural stiffness of the bone. Past the elastic region, a certain amount of force will result in irreversible damage. This is called the yield point, where the curve begins to behave in a non-linear manner. The amount that the bone continues to deform after the yield point is a measure of ductility. Once the applied force reaches the ultimate load, the bone will fail. The amount of work, or energy, required to fail the bone is referred to as toughness. Other parameters that can be calculated from the force-displacement curve include: structural strength, stiffness, deformation, and energy dissipation (16,17).

The force-displacement curve is based on the bone structure as a whole and is dependent upon the mass, geometry, and mineral properties of the bone. To study only the material properties of the bone, it is necessary to normalize out the effects of geometry. To do this, one must look at strain and stress. Stress is measured in units of force per unit area and strain measures the fractional change in dimension of the loaded body. The force-displacement curve can be converted to a stress-strain curve using the appropriate formulas to change force to stress and displacement to strain. This stress-strain curve represents the material properties of the bone without regard to the bone's geometry or mass, and properties that are analogous to the ones on the force-displacement curve can be derived. These strength terms now apply to the material in terms of stresses. The maximum stress, or ultimate stress, represents the toughness of the material and is equivalent to the total amount of energy absorbed before failure is achieved. Young's modulus, another material property, is defined as the ratio of stress to strain. This can be rewritten as Hooke's Law, or the equation of the linear portion of the stress-strain curve. A larger modulus means that a larger amount of stress is needed to achieve a given level of strain.

1.10 STAT Family

The STAT family is a highly conserved class of transcription factors ranging in size between 750 and 800 amino acid residues in length, further characterized by the presence of the Src homology 2 (SH2) domain and a carboxyl-terminal tyrosine phosphorylation site. The SH2 domain is required for STAT proteins to bind to receptor motifs and for dimerization (18). Currently, there are seven known mammalian STAT family members that have been discovered and can be mapped to three different mouse chromosomes. STAT1 and STAT4 are found on chromosome 1, STAT2 and STAT6 on chromosome 10, and STAT3, STAT5a, and STAT5b are found on chromosome 11. Most of the STAT proteins participate in host defense and are only expressed in a few cell types, while STAT3 and STAT5 are expressed and function in most cell types(19). No other STAT genes have been discovered in the genomes of unicellular systems, suggesting that the STAT proteins evolved along with the development of multicellular organisms (20).

Experiments designed to understand interferon-induced transcriptional activity helped reveal a novel pathway of signal transduction called the JAK-STAT pathway. The JAK family of kinases, including Jak1, Jak2, Jak3, and Tyk2, vary in size from 120-135 kDa (21). Jaks serve as soluble intracellular tyrosine kinases with their N-terminal half interacting with the associated receptor (20,21). Cytokines play a crucial role in JAK-STAT signaling. The family of cytokines containing the common receptor subunit glycoprotein 130 (gp130) includes interleukin 6 (IL-6), IL-11, leukemia inhibitory factor (LIF), oncostatin M (OSM), ciliary neurotrophic factor (CNTF), and cardiotrophin 1 (CT-1) (20)(Figure 1). These cytokines are of similar molecular mass, about 20 kDa. The gp130 subunit allows for signal transduction that results in similar physiological effects amongst the different cytokines.

This subfamily is referred to as ‘IL-6-type cytokines’ and they all signal through the activation of gp130-associated Janus kinases and the STAT family of transcription factors.

1.11 STAT Signaling

STAT proteins are found in the cytoplasm in their inactive form. Once one of the requisite cytokines binds to its surface receptor, it recruits gp130 to the receptor complex. This recruitment causes the tyrosine residues to become phosphorylated in the cytoplasmic tail of the receptor leading to dimerization, while simultaneously activating the Jak kinases. The phosphorylated tyrosine residues of the gp130 receptor then serve as a docking site for STAT proteins. The SH2 domains of the STAT proteins recognize these phosphorylated tyrosine residues. The Jak kinases are then able to phosphorylate the recruited STAT proteins at their own tyrosine residues near the C-terminus. Consistent with the other STAT proteins, STAT3 is phosphorylated at a particular tyrosine, Y705, and a particular serine, S727 (22). This allows the phosphorylated STAT proteins to detach from the receptor domain, dimerize, and then translocate to the nucleus (Figure 2). Dimerization of STAT proteins is required for DNA binding (18). Once in the nucleus, the hetero- or homodimer of STAT proteins bind to enhancer elements--activating transcription through its interaction with specific DNA sequences of the target genes (20,21,23).

Common results of IL-6-type cytokine activation include cell proliferation, differentiation, and gene activation (20). In certain cell cultures, STAT3 has also been shown to be activated by growth factors, oncogenes, and interferons. The genes that seem to be regulated by STAT3 activation include antiapoptotic and proliferation genes like Bcl-xL, Bcl-2, Fas, Cyclin D1, Survivin, and c-Myc (24). The activation of STAT proteins is transient, and deactivation can occur via many mechanisms, including dephosphorylation in the nucleus and subsequent protein degradation carried out by the ubuiquitin-proteosome pathway (25). Some cancers exhibit constitutively active STAT3 expression that enhances the growth of tumors (26).

1.12 STAT3 Structure

The protein structure of STAT3 is similar to that of the other STAT family members, containing multiple domains, each with a distinct function, as shown in Figure 3. STAT3 contains a highly conserved amino-terminus that is involved in the tetramerization of the protein structure, a DNA-binding domain specific to palindromic regions, an SH2 domain involved in receptor localization and protein dimerization, and a carboxy-terminal domain responsible for STAT activation (22). Through a systematic deletion of domains and site-directed mutagenesis, it was possible to determine how STAT3 is translocated to the nucleus. A coiled-coil domain of STAT3 was found to be responsible for its nuclear translocation. This unique sequence, along with a conserved portion of the DNA binding domain, allows for the nuclear translocation of STAT3 (27). Differences in the activation of different STAT proteins arise from the specificity in the SH2 domain of each STAT protein (28).

1.13 STAT3 Discovery

Among the seven members of the STAT family, STAT3, STAT5a, and STAT5b have been shown to have direct involvement in skeletal development with STAT3 having the most profound effect on bone. STAT3 was first discovered binding to DNA in IL-6-stimulated hepatocytes and identified as acute phase response factor (APRF) because it was specifically found binding with an enhancer element in the promoter region of acute-phase genes. APRF was then purified and cloned from the mouse liver extracts. APRF transcripts were subsequently found in several different tissue types, including heart, brain, placenta, and lung (29).

Universal knockout of STAT3 expression is lethal past embryonic day seven, prior to gastrulation, showing that STAT3 is crucial during early embryonic development, especially for mesoderm formation (30). Up until embryonic day six, the embryos appear normal, suggesting that STAT3 is not required for the formation of the egg cylinder, but nutritional insufficiencies as a result of STAT3 knock-out cause the degeneration of the embryo. STAT3 is the only member of the STAT family whose deficiency leads to the death of the animal. The role that STAT3 plays in tissues must be studied using Cre-loxP recombination systems to conditionally knockout the gene for STAT3 in specific tissues of study.

1.14 Maintenance of Pluripotency in Embryonic Stem Cells

STAT3 is not only required for the maintenance of embryonic stem cells in a pluripotent state, it is also sufficient (31). Self-renewal of the embryonic stem cells is propagated through LIF and other members of the IL-6 family of cytokines. Without STAT3 expression in ES cells, the cells will begin differentiating. These findings are intriguing when paired with the knowledge that STAT3 is known to induce the differentiation of somatic cell types (32).

1.15 Hyper-IgE Syndrome

In 1966, Davis and his colleagues described a case study of two girls with recurring episodes of pneumonia, eczema-like rashes, and recurrent skin boils lacking warmth or tenderness. They termed this condition “Job syndrome” (33). Later, in 1972, Buckley et al. described a similar condition reminiscent of the repeated staphylococcal abscesses seen in Davis’ patients in two adolescent boys, with the inclusion of exceptionally high serum concentrations of immunoglobulin E (IgE) and eosinophilia. The concentrations of the other immunoglobulins were normal. The patients also had marked growth retardation, joint abscesses, and chronic dermatitis (34). High levels of IgE were later found in Davis' patients and these syndromes were merged into one: Hyper-IgE Syndrome (HIES).

Recent genetic studies have linked a homozygous mutation in the tyrosine kinase2 (TYK2) and a heterozygous mutation in the STAT3 gene to be causal in HIES (24,35,36). Holland et al. were the first to discover STAT3's link to HIES. They observed that mononuclear cells from HIES patients stimulated with IL-6 had lower levels of monocyte chemoattractant protein 1. This result suggested a defect in the IL-6-mediated signaling pathway and its downstream effectors, including STAT3. The mutations were found in either the DNA binding region or the SH2 domains of STAT3 (24).

In addition to the immunological manifestations of this syndrome, HIES presents with a range of pleiotropic effects, including craniofacial, dental, musculoskeletal, neurological, and vascular abnormalities (37)(Figure 4). Patients with HIES have notable skeletal abnormalities, including prominent foreheads and chins, deep-set eyes, broad noses, and high arched palates. Most patients also present with recurrent fractures caused by seemingly minor traumas, occurring in the long bones, ribs, and pelvic bones (38). These fractures can be attributed to an enhancement of osteoclastogenesis and osteopenia (39). A hallmark of treatment for HIES is to prevent skin and pulmonary infections with prophylactic antibacterial and antifungal treatment. Bone marrow transplants have been attempted for HIES patients with variable results (37). Cytokine replacement has been proposed as a novel therapy, however it is unclear whether the multiple functions attributed to STAT3 can be compensated for, and even then it appears that the total reversal of HIES is unattainable.

1.16 Regulators of STAT3

As noted earlier, STAT3 activation is a tightly controlled and transient process. There exist many negative regulatory mechanisms that control the activation of STAT3 under normal physiological conditions. These occur at different levels of the signal transduction pathway. There exist two strategies for inhibiting STAT3: indirectly by deactivating the upstream molecules in the JAK-STAT pathway or through direct targeting of the STAT3 protein itself. Activated STAT3 is able to bind to the promotor regions of suppressor of cytokine signaling (SOCS) genes (40). SOCS then go on to interact with the kinase domains of different JAK proteins associated with the membrane-bound receptors leading to the reduction of STAT3 activation. Another molecule, Src homology domain-containing tyrosine phosphatases 2 (SHP-2), is responsible for inactivating JAKs, STAT3, and their associated receptors through SHP-2's interaction with the intracellular domain of the cytokine receptors (41). Pharmaceutical companies have taken an interest in developing small-molecule inhibitors of STAT3 for the treatment of STAT3-associated pathologies, especially cancers (42-44).

1.17 STAT3 in Bone

STAT3, over the other STAT proteins, appears to have the most profound effect on bone homeostasis. Osteoblast cell culture studies have shown that osteoblasts respond to IL-6-type cytokines and signal through the JAK-STAT pathway (45). Further strengthening this result, it was found that all osteoblastic cells have receptors on their surfaces that are capable of responding to all members of the gp130 cytokine sub-family (46). Using a dominant-negative form of STAT3, it was determined that the activation of STAT3 is required for gp130-dependent osteoclastogenesis through its targeting of RANKL expression in osteoblasts (47). The formation of osteoclasts, however, is not fully dependent upon gp130 signaling as evidenced by the presence of osteoclasts in gp130-deficient mice (48). In addition to stimulating the differentiation and proliferation of osteoclasts, STAT3 is able to push osteoprogenitors towards a committed osteoblastic phenotype while indirectly regulating the differentiation of osteoclasts (45). Through conditional targeting of STAT3 in osteoblasts *in vivo,* mice lacking STAT3 expression in osteoblasts demonstrated an osteoporotic phenotype resulting from the lack of osteoblast activity. This implicates STAT3 as having a profound effect on normal osteoblast functioning (49). Recent studies have suggested that gp130 signaling affects bone formation and maintenance primarily via osteocytes, whose job it is to regulate the differentiation of osteoblasts and produce bone matrix (50).

The JAK-STAT signaling pathway has also been implicated in mechanotransduction in bone. When stimulated with fluid shear stress, osteoblastic cells significantly up-regulate the expression of STAT3 30-90 minutes post-loading (51). *In vivo* ulnar loading studies have replicated these results—demonstrating that STAT3 plays a role in bone's responsiveness to mechanical loading.

1.18 Bioinformatic Profiling

Changes in the level of gene expression caused by abnormal level, inappropriate structure, or a non-functioning transcriptional regulator, like STAT3, have been directly linked to a number of human diseases (52). Chromatin immunoprecipitation (ChIP) followed by next generation sequencing (ChIP-seq) selectively enriches for DNA sequences that are bound by a particular protein *in vivo*. First described by Solomon and colleagues in 1988 (53), ChIP-seq is emerging as a widely used approach to map the genomic loci of transcription factor binding, providing increased annotation to the genome of different species. The process of ChIP-seq begins with cross-linking of DNA to DNA-binding proteins *in vivo* through the treatment with formaldehyde. Next, the chromatin is sheared into smaller pieces ranging in size from 200-600 base pairs.

An antibody specific to the protein of interest (STAT3) is used to immunoprecipitate out the DNA-protein complex so that the bound fragments can be sequenced. Most sequences from ChIP experiments go on to be sequenced with Illumina Genome Analyzer.

ChIP-seq offers advantages over its contemporaries, like a higher resolution, fewer artifacts, and greater coverage. Prior methods, like ChIP-chip, were severely limited by the amount of arrays that could be sequenced. These improvements allow for more precise mapping of the protein-bound sites within a genome (54). Discovering the genome-wide binding patterns of particular transcription factors can be immensely useful when a systems-level view of cellular processes being driven by that transcription factor are desired, especially if the absence of that transcription factor, as is the case for STAT3, causes major disruptions to homeostasis.

New techniques, like ChIP-seq, allow for the generation of whole-genome binding patterns of transcription factors and other molecules that interact directly with DNA. The library of genes generated by ChIP-seq is first aligned to a reference genome, usually mouse or human. Once the enriched sequences have been aligned, the location of the nearest gene loci can be determined and quantified; this will give insight into the transcription factor’s mechanism for regulating certain genes. The main disadvantage of ChIP-seq experiments is the current cost and availability. The associated costs with ChIP-seq include those for machine depreciation and reagent costs (54). The ChIP portion of the experiment requires about 10^7 cells, which will yield about 10-100 ng of DNA.

Kang and colleagues performed a meta-analysis of STAT protein ChIP-seq experiments in order to elucidate the genome binding behaviors of STAT proteins. They found that the ability of any given STAT protein to bind DNA is primarily determined by the particular cell type being studied rather than the STAT protein being studied. For example, STAT3 and STAT5 have more shared binding sites in T cells than STAT5 in T cells has in common with binding sites in non-T cells (55). STAT proteins recognize and bind very similar, and in some cases identical, DNA sequence motifs, yet they are still able to elicit pleiotropic effects *in vitro*. Recently, genome-wide analysis of STAT3 binding sites was performed to better understand its role in the anti-inflammatory response in macrophages. IL-10, an anti-inflammatory cytokine, signals through the JAK-STAT3 pathway to stimulate the transcription of genes that will in turn suppress the pro-inflammatory cytokines. The further examination of these putative downstream targets of STAT3 will help to reveal potential anti-inflammatory treatments once the whole signaling network has been characterized (56).

In order to better understand what actions the downstream effectors of STAT3 signaling participate in to generate the bone phenotypes, we have mined data from the Mouse Encyclopedia of DNA Elements (ENCODE) Consortium for transcription factors (57). The ENCODE database project was developed with the intentions of providing researchers with a novel understanding of the human genome in the context of its biological functionality and indeed had fulfilled this goal by generating a catalogue of potential functional elements in the genome of multiple species (57,58). Elucidating the transcriptional regulatory elements that are responsible for the expression of each transcript poses a significant challenge, especially when faced with the complexity of cellular processes that a few transcripts can control. These types of whole genome analyses are mainly exploratory in nature but are still helpful in understanding biological phenomena in the context of gene regulation. The evaluation of the meaning of the output of gene lists from ChIP-seq experiments requires the support of bioinformatics software packages, such as Ingenuity Pathway Analysis (IPA) and DAVID (the database for annotation, visualization, and integrated discovery). DAVID is especially useful because of its ability to handle any type or format of gene lists, regardless of which software package generated them.

1.19 Research Goals

Bone cells serve not only a biomechanical support function; they also take part in a homeostatic role by responding to local cytokines and circulating hormones. Osteoclasts and osteoblasts work in sequence to accomplish bone remodeling and it is this series of events that must be finely orchestrated, otherwise pathologies arise. It is our goal to target this imbalance in bone remodeling to correct skeletal pathologies, but first we must elucidate the basic molecular interactions in bone formation and depletion. The JAK-STAT pathway is known to play a crucial role in the growth and differentiation of many cell types, including bone cells. STAT3, specifically, has a more profound effect on bone than the other STAT family of proteins. Through conditional knock-out studies in mice models, our lab has shown that STAT3 is particularly important in mechanotransduction. Recently, our lab has established an immortalized STAT3 KO cell line derived from bone marrow stromal cells using CRISPR/Cas9. This cell line enables us to examine STAT3's role in differentiation and proliferation of bone progenitor cells *in vitro*. We therefore hypothesize that STAT3 also affects osteoblast differentiation and subsequently early skeletal development. In order to test this hypothesis, this study explores three specific aims: 1. to determine the role of STAT3 in skeletal development using an early-osteoblast-specific conditional STAT3 cKO mouse model with newborn and 8-week old mice, 2. to study STAT3's role in osteoblast differentiation and proliferation *in vitro*, and 3. to characterize the whole-genome binding patterns of STAT3 in order to find novel downstream targets of STAT3 signaling that could explain the skeletal phenotypes observed in our STAT3 cKO mice.

CHAPTER 2. MATERIALS AND METHODS

2.1 Newborn cKO Mice

To further understand the pre-osteoblast-specific STAT3 knockout phenotype, whole skeletons of newborn mouse pups were stained to visualize the amount of mineralized tissue compared to the amount of cartilage tissue present. Experimental mouse pups were bred using the same schematic for the 8-week old mice described below. The mice were collected from their cages between 0 and 36 hours post-partum and were euthanized using isopropanol inhalation. The pups were visually assessed for gender via the presence or absence of scrotal pigmentation (59)(Figure 5). Because skin can block the penetration of the stains, the mice were skinned and eviscerated. The right limbs were removed to aid in imaging of the skeleton, and a piece of calcified tissue from the forelimb was extracted and processed for PCR, as described for the tail snips below. All the proceeding steps were performed on the shaker at RT. The pups were fixed in 95% ethanol overnight or up to two days. Next, lipids were removed by immersing them in acetone overnight before beginning the staining process. The pups were then immersed in a staining solution comprised of one volume 0.3% alcian blue 8GX (dissolved in 70% ethanol), one volume 0.1% alizarin red (dissolved in distilled water), one volume glacial acetic acid, and 17 volumes 70% ethanol. The pups were left to stain for 2-3 days or until the dye fully penetrated into the calcified tissue. After washing with 95% ethanol for one hour, the muscles were rendered clear using 1% KOH, which was changed every day until the muscles were completely clear. Lastly, the pups were passed through a series of glycerol/KOH washes and then stored in 80% glycerol. For long-term storage, KOH would leach out the dyes from the skeletons. Alizarin red staining stains hydroxyapatite crystals in bones while alcian blue stains glycosaminoglycans in cartilage tissues (60-62). All pups were imaged using a Stereologer system (Stereology Resource Center,Chester, MD) on a Nikon SMZ1500 microscope.

PCR amplification and identification of the Osx-cre and STAT3 genes was performed as described below. Sex genotyping of the newborn pups was performed to confirm the gender of the newborn pups. Primers were designed based on the highly homologus SMC genes that are found on the X (X chromosomal SmcX) and Y (Y chromosomal SmcY) chromosomes. Primer sequences were as follows: SMCX-1 5'- CCGCTGCCAAATTCTTTGG -3' and SMC4-1 5'- TGAAGCTTTTGGCTTTGAG -3'. The PCR product for female mice was a single band 350 bp in length while the males produced two bands, 300 bp and 350 bp in length (Figure 6). The Y-linked copies of the SMC genes have evolved 1.8 times faster than their X homologs accounting for an intron difference between the two (63).

The thermal cycles were ran as follows: 94°C for 3 minutes, 35 cycles of 94°C for 30 sec., 54°C for 30 sec., 72°C for 30 sec., followed by one cycle of 72°C for 7 minutes.

2.2 8-week Old Conditional STAT3 Knockout Mice

2.2.1 Experimental Animals

All mice studies were reviewed and approved by the Indiana University Animal Care and Use Committee (IUACUC). Osteoblast-specific STAT3 knockout mice were generated using the cre-loxP recombinase system. Mice with floxed *Stat3* ($\text{STAT3}^{\text{flox/flox}}$) were bred with mice expressing Cre recombinase driven by the promoter for Osterix--only expressed in early osteoblast cells. The STAT3 floxed mice were obtained from Dr. Xin-Yuan Fu in the Department of Microbiology and Immunology, Indiana University School of Medicine and the Osx-cre mice were purchased from Jackson Laboratory (Bar Harbor, ME). The loxP sequences of the STAT3 floxed mice flanked exons 18-20 of the *Stat3* gene. These exons are responsible for encoding the SH2 domain of the STAT3 protein which is required for STAT3 activation (64).

2.2.2 Breeding Scheme

The pre-osteoblast-specific STAT3 knockout (cKO) mice were generated through a two-step process. First, the homozygous Osx-cre transgenic mice were bred with homozygous STAT3$^{flox/flox}$ mice to create F_1 offspring carrying both heterozygous Osx-cre and heterozygous (STAT3$^{flox/+}$) genes in the mice genome. The F1 offspring (Osx-cre; STAT3$^{flox/flox}$) were then bred with each other to produce the F_2 generation. Only two genotypes of the F_2 generation were used: Osx-cre; STAT3$^{flox/flox}$ (cKO mice) and Osx-cre; STAT3$^{+/+}$ (WT mice). It has been reported that Cre expression itself produces a phenotype and recent studies have suggested that Osx-cre expression might produce a phenotype(65). For this reason, we only used Cre (+) WT controls for this study. (Figure 7)

2.2.3 Genotyping Mice

The genotype of the experimental mice was confirmed using polymerase chain reaction (PCR) amplification of tail DNA. Approximately 2 mm was removed from the proximal tip of the tail and stored in a 1.5 mL microcentrifuge tube. Scissors were sterilized in between each mouse using 70% ethanol. The tails were immersed in a lysis buffer solution with 50 mM Tris, 50 mF KCL, 2.5 mM EDTA, 0.4% NP-40, and 0.45% Tween-40. 0.4 mg/mL of proteinase K was added to the lysis buffer immediately before use. 100 µL of the lysis buffer: proteinase K solution was alliquoted into each 1.5 mL microcentrifuge tube containing the tail snip and allowed to incubate in a 56°^{C} water bath overnight. The next day the tubes were were transferred into a 95°^{C} dry bath for 10 minutes to deactivate the proteinase K. The DNA tubes were then diluted with 100 µL autoclaved miliQ water. 1 µL of this DNA solution was then added to a PCR tube containing 12.5 µL REDTaq ReadyMix (Sigma-Aldrich, St. Louis, MO, USA), 5.5 µL sterile PCR water, 0.5 µL (0.5 µM) forward primer, and 0.5 µL (0.5 µL) reverse primer for a total of 20 µL. Primer sequences used for amplification of STAT3 and Osx-cre are as follows: Stat3 forward 5'-ATT GGA ACC TGG GAC CAA GTG G-3', Stat3 reverse 5'-ACATGT ACT TAC AGG GTG TGT GC-3', Osx-cre forward 5'- CTC TTC ATG AGG AGG ACC CT -3', Osx-cre reverse 5'- GCC AGG CAG GTG CCT GGA CAT -3'. The PCR tubes were then ran in a PTC-11 Peltier Thermal Cycler for 39 cylces (1 min at 94°C, 30 sec at 94°C, 30 sec at 55°C, and 30 sec at 68°C). The PCR tubes were then removed from the thermal cycler and loaded into a 2.5% agarose gel with 1x SYBR safe DNA stain (Life Technologies Corporation, Carlsbad, CA, USA). The samples were run alongside a 100 bp ladder. After gel electrophoresis, the gel was imaged using a Typhoon FLA 9500 scanner.

The presence of a 615 bp DNA band (Cre-recombinase) indicated that the mice were carrying the Cre transgene (Figure 8). Because Cre is not an endogenous gene normally expressed in mammalian species, the absence of this band meant that the mouse was not carrying the Cre transgene. The primers for STAT3 amplification were designed to flank the loxP site upstream and downstream the

STAT3 gene sequence, therefore allowing differentiation of STAT3 WT and cKO. PCR amplified a 520 bp DNA band for STAT3$^{flox/flox}$ mice and a 480 bp DNA band for STAT3$^{+/+}$ mice (Figure 8). Both the 520 and 480 bp DNA bands were amplified for STAT3$^{flox/+}$ mice but these mice were only used for colony maintenance and not experimentation. The expression of Cre was limited to pre-osteoblast cells and therefore STAT3 was conditionally knocked-out.

2.2.4 Animal Sacrifice

One week prior to sacrificing, the experimental mice were injected intraperitoneally with calcein (green fluorochrome label, 30 mg/kg body weight, Sigma-Aldrich) and then with alizarin (red fluorochrome label, 50 mg/kg body weight, Sigma-Aldrich) two days before sacrifice. Calcein and alizarin label incorporate into actively mineralizing bone but have a short half-life *in vivo*, making them an ideal system to label newly formed bone. Once they reached eight weeks of age, the experimental mice were first weighed and then were euthanized with CO_2 inhalation followed by cervical dislocation as a secondary means of euthanasia. The left femurs were extracted, stripped of soft tissue, wrapped in 0.85% saline-soaked gauze and stored at -20°C. The right femurs were extracted, stripped of soft tissue, and immersed in 10% neutral buffered formalin for fixation overnight. A piece of tail was also removed to run a confirmatory PCR genotype.

2.2.5 Bone Mineral Density (PIXImus)

Bone mineral density (BMD, g/cm^2) and bone mineral content (BMC, g) were determined for the left femurs of the experimental mice. BMD and BMC were measured and calculated by using peripheral dual-energy X-ray absorptionmentry (pDXA, PIXImus II, GE-Lunar Co.).

2.2.6 Micro-Computed Tomography (Micro-CT) Analysis

The left femurs of the 8-week old STAT3 WT and cKO mice were slowly brought to room temperature from -20°C and then wrapped in parafilm to keep them from drying out during the scanning process. The femurs were positioned and stabilized in Styrofoam and mounted on the micro-CT platform for scanning (SkyScan 1172, Bruker-microCT, Kontich, Belgium). Scanning parameters were set as follows: voltage: 60kV, resolution: 12 µm, binning mode: 2K, filter: Al 0.5 mm, rotation step: 0.7°, and averaging frame: 2. The femur specimens were rotationally scanned for 180° to generate raw projection images per rotation step (0.7°). Once scanned, the raw images were reconstructed using the SkyScan NRecon software (Bruker-microCT, Kontich, Belgium) using the following parameters: Post alignment: variable, Smoothing: 2, Ring artifact reduction: 5, Beam hardening: 20, Threshold: 0-0.11 (could differ by study) and File format: BMP. The reconstruction process rendered the images into their three-dimensional structure allowing for further quantitative analysis using SkyScan CT-Analyser (CTAn) (Bruker-microCT, Kontich, Belgium) software analysis. Trabecular analysis was performed on a 0.5 and 1.0 mm thick section 1.0 mm proximal to the distal growth plate. Bone Volume/Tissue Volume (BV/TV), Trabecular Bone Thickness (Tb.Th), Trabecular Bone Number (Tb.N), and Trabecular Bone Separation (Tb.Sp) were calculated. Cortical analysis in the femoral midshaft region was performed on a single slice with the region of interest set to exclude all trabecular bone.

Three dimensional representations of the midshaft cortical, proximal ⅓ cortical, and distal trabecular regions were generated by first selecting the region of interest in the SkyScan CT-Analyser software and then exporting as “3D model” in the binary images view. The file was then opened in the Skyscan CT-vol program for 3D manipulation and imaging.

2.2.7 Biomechanical Testing

After micro-CT scanning was complete, the left femurs were subjected to 3-point bending (the femurs did not meet the minimum span requirements for 4-point bending). The femurs were slowly brought to room temperature from -20°C and then immersed in phosphate buffered saline (pH 7.4) inside petri dishes to keep them from drying out until the test was completed. The shortest femur (11.25 mm) was used to set the limiting bone span between the bottom two points of the loading apparatus. The span was set at 7.02 mm with the top point set at the center, 3.51 mm. The femurs were loaded anterior side upward onto a Bose ElectroForce 3200 Test Instrument, pre-loaded to a force of 0.2-0.5 N, pre-conditioned for 8 cycles (2 Hz), and then monotonically tested to failure at a rate of 0.025 mm/s up to 30 N or failure. During each bending test, the load and deformation were recorded every 0.04 seconds. From these recordings, structural strength (yield force and ultimate force), stiffness (the slope of the linear portion of the force vs. displacement curve), and deformation (yield deformation, failure deformation and post-yield deformation) were derived at the whole bone level (66,67). The point of fracture initiation was noted and measured on the anterior face from the proximal end of the femur.

To derive structural-level mechanical properties, the micro-CT data from the same femurs was used to normalize the geometry of the bones. The 3D reconstructions of the left femurs were opened in Data Viewer and reoriented with the anterior side to the right and the midshaft straightened so that the mediolateral axis coincided with the x-axis. 7 slices from the failure site (3 slices proximally, 1 slice at failure site, and 3 slices distally) were imported and analyzed using SkyScan Software CTAn. The images were saved in binary format with a threshold of 70-255 and analyzed using a MATLAB script written by Professor Joseph Wallace at Indiana University-Purdue University Indianapolis, Department of Biomedical Engineering (BME) and edited by BME graduate student Michael Ryne Horn and BME undergraduate student Alycia Berman.

Through the MATLAB script, a failure point was defined and an initial point was selected to avoid the ‘toe-in’ region. The script also required a selection of the linear portion of the curve with a 0.2% strain offset. The MATLAB script correlates the force-displacement curve with the micro-CT data at the failure site in order to derive material properties of the femur by transforming it into a stress-strain curve. Bone material properties were calculated such as: ultimate stress (the highest force per area of a material can hold before failure), ultimate strain (maximum deformation representing the bending displacement relative to two bottom point span), Young’s modulus (the slope of the linear region of the stress-strain curve), and total toughness (the area under the stress-strain curve).

2.2.8 Histology

After being immersed in 10% neutral-buffered formalin overnight, the right femurs of the 8-week old WT and cKO mice were cut into a distal and midshaft portion and stored in 70% ethanol until processing. Once ready, the femurs were dehydrated through a graded series of ethanols before being cleared in xylene, 2-8 hours per step, under vacuum. The femurs were then infiltrated with a 1:1 solution of methyl methacrylate (MMA) and 100% ethanol for 2-8 hours and then undiluted MMA for another 2-8 hours. Next, the femurs were infiltrated with unpolymerized MMA with 4% dibutyl phthalate, a softening agent, for up to one week under vacuum. The vacuum was necessary to completely remove trapped air bubbles from the bone samples. Once fully infiltrated, the distal femurs were embedded in a mixture of MMA, 4% dibutyl phthalate, and 0.25% Perkadox 16, a catalyst, and allowed to sit under vacuum for at least 2 hours before capping the vial. The vials were then left to refrigerate overnight and then polymerized at room temperature until completely solid. The midshaft portions of the femurs were infiltrated and embedded in a similar manner but were placed in a glass tube to polymerize. The polymerized blocks containing the distal femurs were removed of excess plastic using a band saw and further shaped using a dental model trimmer. Thin sections (4 μm) of primarily cancellous bone were cut using a rotary microtome outfitted with a tungsten-carbide knife. A total of five sections from each mouse were obtained: two unstained slides for fluorescent label scoring, one TRAP slide for osteoclast scoring, one VKM slide for osteoblast scoring, and one unstained slide to serve as a spare. Upon polymeriziation of the midshaft portions of the femurs, the glass tubes were broken and removed. Thick sections (75-100 μm) in the midshaft region were cut using a diamond wire saw (Histo-saw, Delaware Diamond Knives, Wilmington, DE) and, when necessary, ground to their final thickness of 50 μm using 600 grit wet/dry silicon carbide sandpaper (LECO). Three thick sections from each mouse were collected and cover-slipped with Eukitt mounting reagent to be scored for cortical parameters.

2.2.9 Dynamic Histomorphometry

Thin sections of trabecular bone at the distal femur of 8-week old WT and cKO mice were left plasticized and cover-slipped using Eukitt mounting reagent. The fluorescent, calcein and alizarin, labels were then visualized using an Olympus BX53 light/fluorescent microscope and Olympus DP72 camera interfaced with Osteomeasure™ software version 1.01 (OsteoMetrics Inc, Decatur GA). An area 0.4 mm proximal to the growth plate and 0.5 mm medial to the endosteal surface of the cortical bone was measured (approximately 0.6 mm^2 area in total). All measurements were taken at 200x magnification under fluorescent light and abbreviations were ascribed according to Parfitt et al. (68).

Thick sections of cortical bone from the midshaft region were also left unstained and scored at 200x magnification. Both the periosteal and endosteal bone surfaces were measured. Bone parameters measured included total bone perimeter, single labeled perimenter, double labeled perimeter, and inter-labeled width. These primary data were used to calculate the following: MS/BS = [(dL.Pm+(1/2sL.Pm))/B.Pm × 100 (%)], MAR = Ir.L.Th/5 days (µm/day) and BFR/BS = MAR × MS/BS × 365 (µm3/µm2/year).

2.2.10 Static Histomorphometry

For static histomorphometry, the thin sections of trabecular bone from the distal femurs were deplasticized in acetone and then stained by two different procedures: (1) a modification of the Von Kossa/MacNeal's (VKM) Tetrachrome protocol and (2) a tartrate-acid resistant acid phosphatase (TRAP) stain (60). VKM staining allows for discrimination between mature, mineralized bone (black) and osteoid (pale blue), helping to reveal osteoblast cell morphology. A TRAP stain marks area of osteoclast activity with a red color and counterstains their nuclei with toluidine blue (69).

2.2.11 TRAP Staining

For thin sections undergoing TRAP staining, the slides were first deplasticized in acetone and rehydrated through a series of ethanols (3 minutes per alcohol change). The slides were then pre-incubated in sodium acetate buffer (pH 5.0) containing 0.2 M sodium acetate and 50 mM sodium tartrate dibasic dehydrate for 20 minutes at room temperature (RT). Slides are then switched to a sodium acetate buffer solution containing 0.2M sodium acetate, 50mM sodium tartrate dibasic dihydrate, 0.5mg/mL napthol AS-MX phosphate, and 1.1 mg/mL fast red TR salt for 1 hour at 37°C. After the hour-long incubation, the thin sections were counterstained with toluidine blue. Once complete, the slides were cover-slipped with an aqueous-based mounting media. The TRAP stained slides were measured for osteoclast activity under bright field at 200x magnification in an area 0.4mm proximal to the distal growth plate. The following primary data were collected through the OsteoMeasure system: Tissue Area (T.Ar), Bone Area (B.Ar), total perimeter (B.Pm), Osteoclast number (N.Oc), and Osteoclast surface (Oc.S). From those primary data, the quantified data were derived: Bone Volume/Tissue Volume (BV/TV) = B.Ar/T.Ar (%), Osteoclast surface/Trabecular Bone surface (Oc.S.BS) = Oc.S/B.Pm (%), and Osteoclast number/Trabecular Bone surface (N.Oc/BS) = N.Oc/B.Pm (#/mm).

2.2.12 VKM Staining

For thin sections receiving VKM staining, sections were deplasticized and rehydrated with the same procedure as TRAP staining mentioned earlier. Slides were then stained in a 5% silver nitrate solution for 10 minutes in the dark, rinsed in distilled water 3 times, and stained in a sodium carbonate-formaldehyde solution containing 5% sodium carbonate and 25mL formaldehyde per 100mL of staining solution. Slides were then rinsed twice and transferred to Farmer’s diminisher solution with potassium ferricyanide for 30 seconds and then washed in running tap water for 20 minutes. After washing, sections were rinsed in distilled water for one minute and then stained in a 2% MacNeal’s tetrachrome solution for 20 min. Sections were rinsed 3 times after staining, dehydrated in a graded series of ethanols, and cleared using two changes of xylenes. Sections were then cover-slipped using a xylene-based mounting media. The VKM slides were measured for osteoblasts under bright field at 200x magnification in an area 0.4 mm proximal to the distal growth plate.

2.3 Immortalized STAT3 Cell Line

2.3.1 Immortalization

Bone marrow stromal cells (BMSC) were immortalized utilizing mTERT by the Bidwell Laboratory (70). After being harvested from the femurs of 6-8-week old mice, the BMSCs were seeded at 6,000 cells/mm^2 and maintained in α–MEM culture medium for 10-14 days before being exposed to the viral supernatant. Surviving cells were selected, isolated, and expanded.

2.3.2 CRISPR

Once immortalized, the WT BMSCs were modified using the CRISPR/Cas9 gene editing tool (71). An oligonucleotide was designed to target the second exon of the *Stat3* gene (Figure 9) and annealed to a linearized vector pX30/BbsI (Addgen). pX330 expresses the Cas9 gene and the single guide RNA. The cultured cells were then screened using PCR and DNA sequencing to identify and isolate STAT3 knock-out cell lines.

2.3.3 Western Blot

Western blot was used to verify the successful deletion of *Stat3* expression in the immortalized STAT3 KO cell lines. The cultures from both the immortalized WT and KO cell lines were harvested and total protein was isolated. Protein samples were then added to a sample buffer and reducing agent mixture. Protein samples were then loaded into a NuPage gel and ran in the electrophoresis apparatus at 200 V for 35 minutes. The protein was then transferred to a nitrocellulose membrane within a Western blot module and ran at 30 V for one hour. The membrane was then blotted with a total anti-STAT3 primary antibody (Cell Signaling Technologies, #9132) and GAPDH secondary antibody (Sigma, G9545) and then the membranes were developed.

2.3.4 Proliferation

Immortalized WT and STAT3 KO BMSCs were seeded at an initial density of 100,000 cells/well in a 6-well culture dish. Cells were cultured for 72 hours in α-MEM medium with 10% FBS. Cells were then counted after the 72 hours using a hemacytometer.

2.3.5 Fluid Shear Stress and RT-qPCR

WT and KO STAT3 BMSCs were seeded on type I collagen-coated slides. One day prior to fluid shear stress (FSS), the cells were starved with 0.2% FBS in α-MEM media. The next day, the glass slides were loaded cell side down into the fluid flow apparatus and loaded at 12 dyn/cm^2 for 30 minutes. The RNA was then collected from both the WT and KO FSS slides as well as WT and KO non-loaded controls. Non-loaded controls were kept in the same incubator under the same conditions as the loaded slides. RNA was isolated using TRIzol Reagent Kit and purified using RNeasy Mini Kit according to manufacturer's protocols. The TRIzol Reagent Kit protocol included steps for homogenization, phase separation, RNA precipitation, and RNA washing. RNA concentration was determined using NanoDrop. Next, cDNA was synthesized from the RNA using Superscript III mix and remaining RNA removed using RNase. The cDNA was then used in a RT-qPCR protocol using SYBR Green PCR Master Mix (Applied Biosystems, Cat. NO: 4367659) using primers for both Wnt3a and Wnt5a (Wnt3a Forward: CTCCTCTGCAGCCTGAAGC, Wnt3a Reverse: GTGGACGGTGGTGCAGTT; Wnt5a Forward: GTGGTCGCTAGGTATGAATAA, Wnt5a Reverse: CGCGTATGTGAAGGCCGTC).

2.3.6 Alkaline Phosphatase Staining

A modified version of the Sigma Alkaline Phosphatase Staining protocol was utilized to stain the immortalized WT and KO BMSCs. BMSCs were cultured in osteogenic media containing ascorbic acid and dexamethasone. Upon nearing confluency, the cells were fixed using 4% PBF and then incubated in an alkaline dye mixture containing Fast Blue RR Salt and Napthol AS-MX Phosphate Alkaline solution for 30 minutes in the dark. Lastly, the cells were incubated in Mayer's Hematoxylin solution to counterstain and then evaluated microscopically for regions of alkaline phosphatase staining.

2.4 Bioinformatic Profiling

First, the peak files (Narrow Peak file format) were downloaded from the ENCODE database from each cell line used. Narrow Peak file format is a format defined by the UCSC ENCODE project and includes the peak loci and chromosome number. PeakAnnotator software was then used to upload the associated BED files and the reference genome, in our case human genome 19, the most recent assembly. BED files contain the coordinates of the peaks contained within the original Narrow Peak files. By utilizing PeakAnnotator software, the peak files were annotated to the closest transcription start site and the nearest gene to that particular TSS. Enriched sites are scored based on the false discovery rate (FDR), which is equivalent to the proportion of misidentified sites found among those that are found to be significant. Also given is the q value of a peak. This q value represents the minimum FDR at which a peak is considered significant and can be compared to a p value when testing a single hypothesis (54).

Basic analysis can be performed with the output of gene lists from ChIP-seq experiments in the ENCODE database, like how far the peak is from a known transcription start site and from exon-intron boundaries. Pathway analysis was run using QIAGEN's Ingenuity Pathway Analysis (IPA®, QIAGEN Redwood City, www.qiagen.com/ingenuity) and additional gene ontology was analyzed using DAVID (72). DAVID works by first inputting the list of overlapping genes that STAT3 was found binding to into the Functional Annotation tool. Official Gene Symbol was selected as the identifier of the input gene list. *Homo sapiens* was then chosen from the species list since all three cell lines were derived from human tissues.

2.16 Statistical Analysis

All data are reported as mean ± S.E.M. (standard error of the mean). The differences between groups were tested using a 2-sample t-test using the Minitab (Minitab Inc. PA) software. Statistical significance was assumed if $P < 0.05$.

CHAPTER 3. RESULTS

3.1 Diaphonization

As a preliminary method to study the role that STAT3 plays in early osteoblast cells, we used whole skeletal preparations of alizarin red/alcian blue stained STAT3 WT and cKO newborn pups. This type of skeletal prep allows for the visualization of differences in bone tissues, such as shortened long bones, widened cartilaginous growth plates, delays in mineralization, and ectopic areas of mineralization. The results of this portion of the study were inconclusive, as there were not any noticeable differences between the ratios of mineralized to non-mineralized tissue when comparing the skeletons of the WT and cKO newborn pups (Figures 10 & 11).

3.2 8-week Old cKO Mice

3.2.1 Phenotypes of Conditional STAT3 Knockout Mice

Through the breeding scheme described previously, 5 male WT, 3 male cKO, 6 female WT, and 5 female cKO mice were generated. There were no significant differences between the body weights of the WT and cKO mice at 8-weeks of age. The male cKO mice trended towards decreased body weight, however it did not reach significance. Body weight values were as follows: male WT 19.98 ± 1.58 g, male cKO 16.40 ± 2.06 g, female WT 18.22 ± 0.25 g, and female cKO 20.14 ± 0.66 g (Figure 12). Male STAT3 cKO mice demonstrated a 12.25% significant decrease in femur length ($p < 0.05$) (Figures 13 & 14). WT male mice femurs were 13.80 ± 0.35 mm while the cKO femurs were 12.11 ± 0.59 mm in length. The female cKO mice had a 5.18% increase in femur length that did not reach significance.

At 8 weeks of age, the pre-osteoblast specific STAT3 knockout male mice demonstrated a significant decrease in bone mineral density while the female cKO mice had a slight increase. The WT males (0.052 ± 0.0007 g/cm^2) had almost 20% more BMD than their male cKO (0.041 ± 0.002 g/cm^2) littermates (Figure 15). Bone mineral content was also measured using PIXImus. When compared as a ratio of bone mineral content to bone area, the male cKO mice also showed a 12% decrease (BMC/area: male WT 0.052 ± 0.0007 g, male cKO 0.046 ± 0.002 g) (Figure 16).

3.2.2 Micro-CT

The male and female cKO mice both showed slightly decreased Bone Volume/Tissue Volume (BV/TV) in the distal trabecular region but neither reached significance when analyzing either a 0.5 or 1.0 mm thick section of trabecular bone. The other trabecular parameters in the distal femur region (trabecular thickness, number, and separation) were also not significantly different.

Cortical bone analysis in the midshaft region revealed male STAT3 cKO mice to have significantly reduced BV/TV, but showed little to no differences in other parameters such as mean polar moment, tissue volume, and bone volume. Interesting differences, however, arose when the cortical bone in the proximal ⅓ of the femur was analyzed. Male cKO mice had a 48% decrease in bone volume (Figure 17) (male WT 0.013 ± 0.0009 mm^3, male cKO 0.006 ± 0.0006 mm^3) but showed a 2% increase BV/TV (male WT 96.28 ± 0.64 %, male cKO 98.56 ± 0.41 %) (Figure 18).

These differences in structure can be visualized in the 3 dimensional models of all four genotypes in Figure 19. As shown, the male STAT3 cKO mice present with a severe phenotype with cortical widening in the proximal ⅓ region.

3.2.3 Trabecular Bone Histology

Histological analysis in the distal trabecular region of the femurs included the measurement of fluorochrome labels, TRAP stain, and VKM stain. Examining the calcein and alizarin labels showed no significant differences in the bone formation rate between cKO mice and their WT controls (Figure 21). The conditional knockout male mice had a 20% decrease in BFR/BS while the female conditional knockout mice showed only a 3% decrease in BFR/BS. Though not significant, the STAT3 cKO mice of both genders showed decreases in single and double labeled perimeter, as well as decreases in interlabel thickness and mineral apposition rate (Figure 20).

Data from the TRAP stained slides from the distal trabecular region showed a significant increase in the number of osteoclasts present on the surface of the trabecular bone in the male STAT3 cKO mice (Figure 22). The male cKO mice (N.Oc. 27 ± 2) had 40% more osteoclasts than the male WT mice (N.OC. 16 ± 2.01). The female STAT3 cKO mice showed no differences from their WT counterparts. The male STAT3 cKO mice had a 60% increase in the amount of osteoclast surface/bone surface (Oc.S/BS: male WT 6.70 ± 1.057 mm, male cKO 17.612 ± 3.68 mm). Calculations of the amount of osteoclast number/tissue area (N.Oc./T.Ar) and the amount of osteoclast number/bone perimeter (N.Oc./B.Pm) showed similar results, with the male STAT3 cKO mice exhibiting a 40% increase in N.Oc./T.Ar and a 50% increase in N.Oc./B.Pm. Male and female STAT3 cKO mice both showed a decrease in the number of osteoclasts/osteoclast perimeter; however, these differences did not reach a significant level.

Data gathered from the VKM stained slides from the distal trabecular region showed a significant difference in osteoid volume/bone volume (OV/BV) and osteoid surface/bone surface (OS/BS) (Figure 23).

Male STAT3 cKO mice had increased amounts of OV/BV and OS/BS while the other bone parameters showed no significant difference.

3.2.4 Cortical Bone Histology

Cortical bone size and growth rate was analyzed in the femoral mishafts of the 8-week old STAT3 WT and cKO mice by examining cross-sectional slices for their fluorochrome labels. Differences arose between the STAT3 WT and cKO in cortical bone volume/tissue volume (Ct.BV/TV) and periosteal double-labeled perimeter (Ps.dL.Pm). Male STAT3 cKO mice had a 10% decrease in Ct.BV/TV (male WT 46.95 ± 0.339%, male cKO 41.961 ± 1.596%) and a 121% increase in Ps.dL.Pm (male WT 0.197 ± 0.0235 mm, male cKO 0.437 ± 0.138 mm) (Figure 24). All the other cortical bone parameters, including single label perimeter on both periosteal and endocortical surfaces, showed no significant differences between the WT and cKO mice of both genders.

3.2.5 Mechanical Testing: 3 Point Bending

The left femurs from 8-week old pre-osteoblast-specific STAT3 WT and cKO mice were subjected to 3 point bending to determine their strength. The femurs of the male cKO mice appeared to be weaker and less resistant to fracturing. Male cKO showed a 54% decrease in ultimate force (ultimate force: male WT

13.66 ± 1.90 N, male cKO 6.22 ± 0.99 N), a 57% decrease in stiffness (stiffness: male WT 78.84 ± 9.30 N/mm, male cKO 33.45 ± 7.72 N/mm), a 52% decrease in work to yield (work to yield: male WT 0.594 ± 0.0619 mJ, male cKO 0.284 ± 0.0499 mJ), a 58% decrease in yield stress (yield stress: male WT 110.36 ± 9.90 MPa, male cKO 46.11 ± 7.72 MPa), a 56% decrease in ultimate stress (ultimate stress: male WT 169.40 ± 7.24 MPa, male cKO 74.47 ± 9.29 MPa), and a 71% decrease in Young's modulus (modulus: male WT 6.80 ± 0.523 GPa, male cKO 1.97 ± 0.227 GPa) (Figure 25) . The same parameters for the female WT and cKO mice showed no significant differences. The male cKO mice experienced a 99% increase in total displacement, though the standard deviation was too great for this value to be significant. Male cKO mice had a slight decrease in toughness as compared to male WT mice, but this difference also did not reach a significant level.

3.3 Immortalized STAT3 Cell Line

BMSCs were immortalized using mTERT and then modified using CRISPR/Cas9 editing to ablate the *Stat3* gene. Successful deletion of the Stat3 expression was confirmed using Western Blot analysis and GAPDH as a control (Figure 9). A doubling time experiment was performed on the immortalized WT and KO STAT3 cell lines to analyze their proliferation capabilities. The STAT3 KO cells presented with significantly reduced proliferation rates as compared to the WT control cells (Figure 26). The STAT3 KO cells also showed diminished alkaline phosphatase staining in osteogenic culture media, suggesting a reduced differentiation potential (Figure 27). The immortalized WT and STAT3 KO cells were also subjected to FSS and RT-qPCR analysis of the isolated RNA showed significantly lower levels of both Wnt3a and Wnt5a mRNA (Figure 28).

3.4 Bioinformatic Profiling

Initial browsing of the ‘ENCODE ChIP-seq Experiment Matrix’ revealed that three different cell lines had been examined for STAT3 binding patterns: GM12878, HeLa-S3, and MCF10 cells. All three cell lines are derived from human tissue and no STAT3 ChIP-seq experimental data has been deposited for mouse cell lines. The GM12878 cell line is derived from B-lymphocytes and represents the mesodermal lineage. The HeLa-S3 cell line is from cervical carcinoma cells and represents the ectodermal lineage. Lastly, the MCF10+ cells are derived from non-tumorigenic, epithelial mammary gland tissue, also representing the ectodermal lineage. After generating the peaks from the database the following amounts of peaks were found for STAT3: GM12878 - 6487 peaks, HeLa-S3 - 13,834 peaks, and MCF10+ - 39,908 peaks generated. Of these peaks, 1,709 of them were overlapping peaks from all three cell lines (Figure 29) and these represent the potential target genes for STAT3. The peaks were then narrowed down on the basis of their distance from the nearest transcriptional start site (TSS), within 5,000 base pairs upstream and 2,000 base pairs downstream from the TSS. This honed the list down to 115 peaks. Further pathway analysis of the peaks and their associated gene loci functions best with a reasonable number of genes (100-2,000 genes)(72), so we decided to exclusively use all the peaks that were generated instead of the ones within our defined TSS range.

The 1,709 genes were inputted into Ingenuity Pathway Analysis (IPA) software to learn more about the relationship between them and potential signaling pathway involvement. IPA is able to produce an array of useful data, such as significant networks, top functions, and top canonical pathways. The top canonical pathways potentially regulated by STAT3 were B-cell receptor signaling (40/171), molecular mechanisms of cancer (62/359), ILK signaling (38/181), integrin signaling (39/195), and NRF2-mediated oxidative stress response (35/177) (Table 1). Shown parenthetically is the ratio of STAT3 bound gene loci to genes known to be involved in these top canonical pathways. The top upstream regulators were TP53, NR3CI, PDGF BB, TNF, and NFκB. Recurring gene ontology amongst the list and their number of associated molecules included gene expression (308), cell death and survival (389), cellular development (335), and cellular growth and proliferation (406).

DAVID also uses the KEGG (Kyto Encyclopedia of Genes and Genomes) database. This database is useful for mapping target gene lists to known signaling pathways (72). KEGG analysis within the DAVID database identified the top five most significant putative pathways regulated by STAT3 as pathways in cancer, chronic myeloid leukemia, pancreatic cancer, Jak-STAT signaling, and adherens junction (Table 2). The Wnt signaling pathway was also listed as being potentially regulated by STAT3 (Figure 31).

CHAPTER 4. DISCUSSION

4.1 Differences in Bone Phenotype

Overall, the male STAT3 cKO mice had significantly shortened femur lengths at 8 weeks of age, as compared to the WT controls. The males also had decreased body weights. At the microscopic level, the cKO males had significantly less BMD and BMC/area. The histological analysis also showed that the cKO males showed a significant increase in the number of osteoclasts in the distal femur region. Also, these same mice had less BV/TV in the midshaft cortical region of their femurs. Differences continued to arise between the WT and cKO mice, especially in the male mice, after 3-point bending was performed. The femurs of the male cKO mice were weaker and less resistant to fracturing. Overall, it appears that the female cKO mice were affected very little, if at all, by the loss of STAT3 in pre-osteoblast cells. Although no obvious differences were observed between WT and cKO mice right after birth, a severe phenotype in the male cKO mice was present by 8-weeks of age. The increased number of osteoclasts on the bone surface coupled with decreased osteoblast activity (BV/TV) suggests some interplay between the two cell types. Cell-to-cell connections between osteoblast cells and the progenitors of osteoclast cells are required in order for osteoclast progenitor cells to commit towards osteoclast development (73,74). Also, the two genes required for osteoclast formation, M-Csf and RANKL, are expressed in osteoblasts. The deficiency of STAT3 in our Osx-cre floxed mice might impair differentiation and proliferation of the osteoblasts that jeopardizes the normal functioning of osteoblasts. As discussed earlier, osteoblasts also possess the ability to inhibit osteoclast formation through the actions of osteoprotegerin. It might be possible that the reduction in osteoblast activity is linked to the increase in osteoclast via OPG activity.

A very similar phenotype to our male STAT3 cKO was observed by Zhou and colleagues when they conditionally deleted Osterix at several time points post-natally. They observed large areas of unresorbed calcified cartilage in the area near the growth plate of endochondral bones. This area was intensely mineralized yet had little to no trabeculae with scant osteoid below this zone of hypomineralization. They ascribed this phenotype to the continuous activity of the proliferating chondrocytes at the growth plate causing the accumulation of calcified cartilage (75).

The fact that only male mice lacking STAT3 expression in pre-osteoblast cells had reduced biomechanical properties and a smaller structure suggests a gender-based effect of STAT3 on the quality of the bone matrix.

4.2 *In Vitro* vs. *In Vivo* Differences

Although no significant differences were observed between the WT and cKO newborn pups in terms of mineralization, the *in vitro* studies using immortalized STAT3 WT and KO cell lines showed significant differences. The KO cells had decreased proliferation rates and reduced ability to differentiate down the osteogenic lineage, as assessed through alkaline phosphatase staining. It is possible that there are other genes and protein products that can compensate for the loss of STAT3 expression *in vivo*. Also, the local paracrine action of neighboring cells could be involved in the compensation effect. Further studies using RT-qPCR could screen for potential genes that act as compensators for STAT3 expression in maintaining the normal bone phenotype.

4.3 STAT3's Genome Binding Profile

There have been several studies that suggest that Wnt signaling heavily influences osteoblast differentiation and function. The reinforcement or depletion of β-catenin signaling in osteoblasts specifically causes the decrease or increase or osteoclast-mediated bone resorption, respectively. Our ChIP-seq analysis suggests that STAT3 might play a role in the Wnt-mediated regulation of bone homeostasis (Figure 31).

DAVID analysis listed Nrf2-signaling pathway as being potentially regulated by STAT3 (Figure 30). Nrf2-signaling is also intriguing to our lab in particular because we have ongoing studies looking into the cytoprotective nature of Nrf2, especially in bone, using Nrf2 KO mice. Preliminary data have shown that mice lacking Nrf2 expression globally have significantly lower BMD, BFR, and ultimate force when compared to age-matched littermate wild-type controls (76). The loss of STAT3 could have confounding effects, particularly in bone, if STAT3 activation targets mediators of the Nrf2-signaling pathway.

4.4 Future Directions

The Osx-cre STAT3 floxed study needs to be repeated with larger sample numbers in order to determine whether the observed phenotype in this study is repeatable or even significant. To aide in the production of more experimental mice, an alternative promoter to Osterix could be used to drive the Cre recombinase. Osterix is expressed most robustly during early osteoblast differentiation, meaning the phenotype might not be replicable with a different promoter. If the phenotype is replicable, then further treatment studies could be performed in order to rescue the normal phenotype. It would also be intriguing to perform the same breeding scheme on ovarectomized female mice to see what their bones do without the protective effects of estrogen. In addition to studying the femurs of the experimental mice, other long bones, such as the ulna and tibia, should be analyzed to see if the same bone deficiencies manifest in the same manner as in the femurs. Although it is unlikely that the deficiencies are unique to the femurs, it is interesting that the overall body weight of the cKO mice did not significantly decrease. Once again, the lack of significance could solely be contributed to low sample numbers within the study, however, it will be interesting to look into further. It would also be useful to take a sequence of x-ray images and/or PIXImus scans of the mice at different time points during development to see when the most marked differences occur.

Ideally, the next step would be to run a ChIP-seq experiment for STAT3 using cells from the osteogenic lineage in order to see binding sites from STAT3 directly in bone cells to obtain a clearer picture of STAT3's place in the homeostatic regulatory network of bone. The next step to undertake, with the current data that is available, is an RNA sequencing experiment. RNA-seq would allow a look at the sequence of the transcriptome of bone cells lacking STAT3 expression to see if there truly exists a difference in the expression levels of STAT3 target genes when STAT3 is removed.

LIST OF REFERENCES

LIST OF REFERENCES

1. Burr DB, Allen MR. Bone morphology and organization. Basic and applied bone biology. Amsterdam: Elsevier/Academic Press; 2013. p. 3-25.
2. Dempster DW. Anatomy and functions of the adult skeleton. Primer on the metabolic bone diseases and disorders of mineral metabolism. Washington DC: The American Society for Bone and Mineral Research; 2006. p. 7-11.
3. Doty SB. Morphological evidence of gap junctions between bone cells. Calcified tissue international. 1981;33(5):509-12.
4. Burr DB, Allen MR. Bone cells. Basic and Applied Bone Biology. Amsterdam: Elsevier/Academic Press; 2013. p. 27-45.
5. Komori T, Yagi H, Nomura S, et al. Targeted disruption of Cbfa1 results in a complete lack of bone formation owing to maturational arrest of osteoblasts. Cell. 1997;89(5):755-64.
6. Nakashima K, Zhou X, Kunkel G, et al. The novel zinc finger-containing transcription factor osterix is required for osteoblast differentiation and bone formation. Cell. 2002;108(1):17-29.
7. Koga T, Matsui Y, Asagiri M, et al. NFAT and Osterix cooperatively regulate bone formation. Nature Medicine. 2005;11(8):880-5.
8. Yavropoulou MP, Yovos JG. The role of the Wnt signaling pathway in osteoblast commitment and differentiation. Hormones (Athens, Greece). 2007;6(4):279-94.
9. Day TF, Guo X, Garrett-Beal L, Yang Y. Wnt/beta-catenin signaling in mesenchymal progenitors controls osteoblast and chondrocyte differentiation during vertebrate skeletogenesis. Developmental Cell. 2005;8(5):739-50.
10. Babij P, Zhao W, Small C, et al. High bone mass in mice expressing a mutant LRP5 gene. Journal of bone and mineral research : the official journal of the American Society for Bone and Mineral Research. 2003;18(6):960-74.
11. Matsuo K, Irie N. Osteoclast-osteoblast communication. Archives of Biochemistry and Biophysics. 2008;473(2):201-9.
12. Burr DB, Allen MR. Local bone cell regulation. Basic and Applied Bone Biology. Amsterdam: Elsevier/Academic Press; 2013. p. 47-73.

13. Dougall WC, Glaccum M, Charrier K, et al. RANK is essential for osteoclast and lymph node development. Genes & Development. 1999;13(18):2412-24.
14. Xiong J, O'Brien CA. Osteocyte RANKL: new insights into the control of bone remodeling. Journal of bone and mineral research : the official journal of the American Society for Bone and Mineral Research. 2012;27(3):499-505.
15. Allen MR, Burr DB. Bone Modeling and Remodeling. Basic and Applied Bone Biology. San Diego, CA: Academic Press; 2014. p. 75-90.
16. Burr DB, Allen MR. Skeletal hard tissue biomechanics. Basic and Applied Bone Biology. Amsterdam: Elsevier/Academic Press; 2013. p. 115-30.
17. Martin RB, Burr DB, Sharkey NA. Skeletal Tissue Mechanics. New York: Springer; 1998. xiv, 392 p. p.
18. Shuai K, Horvath CM, Huang LH, Qureshi SA, Cowburn D, Darnell JE, Jr. Interferon activation of the transcription factor Stat91 involves dimerization through SH2-phosphotyrosyl peptide interactions. Cell. 1994;76(5):821-8.
19. Akira S. Functional roles of STAT family proteins: lessons from knockout mice. Stem Cells. 1999;17(3):138-46.
20. Heinrich PC, Behrmann I, Muller-Newen G, Schaper F, Graeve L. Interleukin-6-type cytokine signalling through the gp130/Jak/STAT pathway. Biochem J. 1998;334 (Pt 2):297-314.
21. Schindler C, Darnell JE, Jr. Transcriptional responses to polypeptide ligands: the JAK-STAT pathway. Annu Rev Biochem. 1995;64:621-51.
22. Levy DE, Lee CK. What does Stat3 do? The Journal of Clinical Investigation. 2002;109(9):1143-8.
23. Aaronson DS, Horvath CM. A road map for those who don't know JAK-STAT. Science (New York, NY). 2002;296(5573):1653-5.
24. Holland SM, DeLeo FR, Elloumi HZ, et al. STAT3 mutations in the hyper-IgE syndrome. The New England Journal of Medicine. 2007;357(16):1608-19.
25. Kim TK, Maniatis T. Regulation of interferon-gamma-activated STAT1 by the ubiquitin-proteasome pathway. Science (New York, NY). 1996;273(5282):1717-9.
26. Yu H, Kortylewski M, Pardoll D. Crosstalk between cancer and immune cells: role of STAT3 in the tumour microenvironment. Nat Rev Immunol. 2007;7(1):41-51.
27. Ma J, Zhang T, Novotny-Diermayr V, Tan AL, Cao X. A novel sequence in the coiled-coil domain of Stat3 essential for its nuclear translocation. J Biol Chem. 2003;278(31):29252-60.
28. Zhang X, Darnell JE, Jr. Functional importance of Stat3 tetramerization in activation of the alpha 2-macroglobulin gene. J Biol Chem. 2001;276(36):33576-81.
29. Akira S, Nishio Y, Inoue M, et al. Molecular cloning of APRF, a novel IFN-stimulated gene factor 3 p91-related transcription factor involved in the gp130-mediated signaling pathway. Cell. 1994;77(1):63-71.

30. Takeda K, Noguchi K, Shi W, et al. Targeted disruption of the mouse Stat3 gene leads to early embryonic lethality. Proc Natl Acad Sci U S A. 1997;94(8):3801-4.
31. Matsuda T, Nakamura T, Nakao K, et al. STAT3 activation is sufficient to maintain an undifferentiated state of mouse embryonic stem cells. The EMBO Journal. 1999;18(15):4261-9.
32. Niwa H, Burdon T, Chambers I, Smith A. Self-renewal of pluripotent embryonic stem cells is mediated via activation of STAT3. Genes & Development. 1998;12(13):2048-60.
33. Davis SD, Schaller J, Wedgwood RJ. Job's Syndrome. Recurrent, "cold", staphylococcal abscesses. Lancet. 1966;1(7445):1013-5.
34. Buckley RH, Wray BB, Belmaker EZ. Extreme hyperimmunoglobulinemia E and undue susceptibility to infection. Pediatrics. 1972;49(1):59-70.
35. He J, Shi J, Xu X, et al. STAT3 mutations correlated with hyper-IgE syndrome lead to blockage of IL-6/STAT3 signalling pathway. Journal of Biosciences. 2012;37(2):243-57.
36. Freeman AF, Holland SM. The hyper-IgE syndromes. Immunol Allergy Clin North Am. 2008;28(2):277-91, viii.
37. Sowerwine KJ, Holland SM, Freeman AF. Hyper-IgE syndrome update. Annals of the New York Academy of Sciences. 2012;1250:25-32.
38. Grimbacher B, Holland SM, Gallin JI, et al. Hyper-IgE syndrome with recurrent infections--an autosomal dominant multisystem disorder. The New England Journal of Medicine. 1999;340(9):692-702.
39. Mogensen TH. STAT3 and the Hyper-IgE syndrome: Clinical presentation, genetic origin, pathogenesis, novel findings and remaining uncertainties. Jak-Stat. 2013;2(2):e23435.
40. Naka T, Narazaki M, Hirata M, et al. Structure and function of a new STAT-induced STAT inhibitor. Nature. 1997;387(6636):924-9.
41. Debnath B, Xu S, Neamati N. Small molecule inhibitors of signal transducer and activator of transcription 3 (Stat3) protein. Journal of Medicinal Chemistry. 2012;55(15):6645-68.
42. Zhao M, Jiang B, Gao FH. Small molecule inhibitors of STAT3 for cancer therapy. Current Medicinal Chemistry. 2011;18(26):4012-8.
43. Uehara Y, Mochizuki M, Matsuno K, Haino T, Asai A. Novel high-throughput screening system for identifying STAT3-SH2 antagonists. Biochemical and Biophysical Research Communications. 2009;380(3):627-31.
44. Lavecchia A, Di Giovanni C, Novellino E. STAT-3 inhibitors: state of the art and new horizons for cancer treatment. Current Medicinal Chemistry. 2011;18(16):2359-75.
45. Bellido T, Borba VZ, Roberson P, Manolagas SC. Activation of the Janus kinase/STAT (signal transducer and activator of transcription) signal transduction pathway by interleukin-6-type cytokines promotes osteoblast differentiation. Endocrinology. 1997;138(9):3666-76.

46. Bellido T, Stahl N, Farruggella TJ, Borba V, Yancopoulos GD, Manolagas SC. Detection of receptors for interleukin-6, interleukin-11, leukemia inhibitory factor, oncostatin M, and ciliary neurotrophic factor in bone marrow stromal/osteoblastic cells. The Journal of Clinical Investigation. 1996;97(2):431-7.
47. O'Brien CA, Gubrij I, Lin SC, Saylors RL, Manolagas SC. STAT3 Activation in Stromal/Osteoblastic Cells Is Required for Induction of the Receptor Activator of NF- B Ligand and Stimulation of Osteoclastogenesis by gp130-utilizing Cytokines or Interleukin-1 but Not 1,25-Dihydroxyvitamin D3 or Parathyroid Hormone. Journal of Biological Chemistry. 1999;274(27):19301-8.
48. Kawasaki K, Gao YH, Yokose S, et al. Osteoclasts are present in gp130-deficient mice. Endocrinology. 1997;138(11):4959-65.
49. Itoh S, Udagawa N, Takahashi N, et al. A critical role for interleukin-6 family-mediated Stat3 activation in osteoblast differentiation and bone formation. Bone. 2006;39(3):505-12.
50. Johnson RW, Brennan HJ, Vrahnas C, et al. The primary function of gp130 signaling in osteoblasts is to maintain bone formation and strength, rather than promote osteoclast formation. Journal of bone and mineral research : The Official Journal of the American Society for Bone and Mineral Research. 2014;29(6):1492-505.
51. Zhou H, Newnum AB, Martin JR, et al. Osteoblast/osteocyte-specific inactivation of Stat3 decreases load-driven bone formation and accumulates reactive oxygen species. Bone. 2011;49(3):404-11.
52. Jimenez-Sanchez G, Childs B, Valle D. Human disease genes. Nature. 2001;409(6822):853-5.
53. Solomon MJ, Larsen PL, Varshavsky A. Mapping protein-DNA interactions in vivo with formaldehyde: evidence that histone H4 is retained on a highly transcribed gene. Cell. 1988;53(6):937-47.
54. Park PJ. ChIP-seq: advantages and challenges of a maturing technology. Nature Reviews Genetics. 2009;10(10):669-80.
55. Kang K, Robinson GW, Hennighausen L. Comprehensive meta-analysis of Signal Transducers and Activators of Transcription (STAT) genomic binding patterns discerns cell-specific cis-regulatory modules. BMC Genomics. 2013;14:4.
56. Hutchins AP, Poulain S, Miranda-Saavedra D. Genome-wide analysis of STAT3 binding in vivo predicts effectors of the anti-inflammatory response in macrophages. Blood. 2012;119(13):e110-9.
57. Birney E, Stamatoyannopoulos JA, Dutta A, et al. Identification and analysis of functional elements in 1% of the human genome by the ENCODE pilot project. Nature. 2007;447(7146):799-816.
58. Yue F, Cheng Y, Breschi A, et al. A comparative encyclopedia of DNA elements in the mouse genome. Nature. 2014;515(7527):355-64.

59. Wolterink-Donselaar IG, Meerding JM, Fernandes C. A method for gender determination in newborn dark pigmented mice. Lab Animal. 2009;38(1):35-8.
60. R.K. Schenk AJO, W. Hermann. Preparation of calcified tissue for light microscopy. In: Dickson GR, editor. In Methods of Calcified Tisue Preparation. New York: Elsevier; 1984. p. 1-56.
61. McLeod MJ. Differential staining of cartilage and bone in whole mouse fetuses by alcian blue and alizarin red S. Teratology. 1980;22(3):299-301.
62. Wallin J, Wilting J, Koseki H, Fritsch R, Christ B, Balling R. The role of Pax-1 in axial skeleton development. Development (Cambridge, England). 1994;120(5):1109-21.
63. Agulnik AI, Bishop CE, Lerner JL, Agulnik SI, Solovyev VV. Analysis of mutation rates in the SMCY/SMCX genes shows that mammalian evolution is male driven. Mammalian Genome : Official Journal of the International Mammalian Genome Society. 1997;8(2):134-8.
64. Welte T, Zhang SS, Wang T, et al. STAT3 deletion during hematopoiesis causes Crohn's disease-like pathogenesis and lethality: a critical role of STAT3 in innate immunity. Proc Natl Acad Sci U S A. 2003;100(4):1879-84.
65. Wang L, Mishina Y, Liu F. Osterix-Cre transgene causes craniofacial bone development defect. Calcified tissue international. 2015;96(2):129-37.
66. Wallace JM, Rajachar RM, Allen MR, et al. Exercise-induced changes in the cortical bone of growing mice are bone- and gender-specific. Bone. 2007;40(4):1120-7.
67. Wallace JM, Rajachar RM, Chen XD, et al. The mechanical phenotype of biglycan-deficient mice is bone- and gender-specific. Bone. 2006;39(1):106-16.
68. Parfitt AM. Bone histomorphometry: standardization of nomenclature, symbols and units (summary of proposed system). Bone. 1988;9(1):67-9.
69. Erlebacher A, Derynck R. Increased expression of TGF-beta 2 in osteoblasts results in an osteoporosis-like phenotype. J Cell Biol. 1996;132(1-2):195-210.
70. Alvarez MB, Childress P, Philip BK, et al. Immortalization and characterization of osteoblast cell lines generated from wild-type and Nmp4-null mouse bone marrow stromal cells using murine telomerase reverse transcriptase (mTERT). J Cell Physiol. 2012;227(5):1873-82.
71. Cong L, Ran FA, Cox D, et al. Multiplex genome engineering using CRISPR/Cas systems. Science (New York, NY). 2013;339(6121):819-23.
72. Huang da W, Sherman BT, Lempicki RA. Systematic and integrative analysis of large gene lists using DAVID bioinformatics resources. Nature protocols. 2009;4(1):44-57.
73. Udagawa N, Takahashi N, Katagiri T, et al. Interleukin (IL)-6 induction of osteoclast differentiation depends on IL-6 receptors expressed on osteoblastic cells but not on osteoclast progenitors. The Journal of Experimental Medicine. 1995;182(5):1461-8.

74. Takeda S, Yoshizawa T, Nagai Y, et al. Stimulation of osteoclast formation by 1,25-dihydroxyvitamin D requires its binding to vitamin D receptor (VDR) in osteoblastic cells: studies using VDR knockout mice. Endocrinology. 1999;140(2):1005-8.
75. Zhou X, Zhang Z, Feng JQ, et al. Multiple functions of Osterix are required for bone growth and homeostasis in postnatal mice. Proc Natl Acad Sci U S A. 2010;107(29):12919-24.
76. Sun YX, Li L, Corry KA, et al. Deletion of Nrf2 reduces skeletal mechanical properties and decreases load-driven bone formation. Bone. 2015;74:1-9.

TABLES

Table 1. IPA Top Canonical Pathways

Name	**p-value**	**Ratio**
B Cell Receptor Signaling	3.19E-10	40/171 (0.234)
Molecular Mechanisms of Cancer	3.65E-09	62/359 (0.173)
ILK Signaling	2.13E-08	38/181 (0.21)
Integrin Signaling	5.61E-08	39/195 (0.2)
NRF2-mediated Oxidative Stress Response	3.53E-07	35/177 (0.198)

Table 2. DAVID/KEGG Top Canonical Pathways

Pathway	**% Genes**	**p-value**
Pathways in cancer	3.9	2.0E-7
Chronic myeloid leukemia	1.4	2.2E-6
Pancreatic cancer	1.2	6.2E-5
Jak-STAT signaling pathway	2.0	1.5E-4
Adherens junction	1.2	1.6E-4

FIGURES

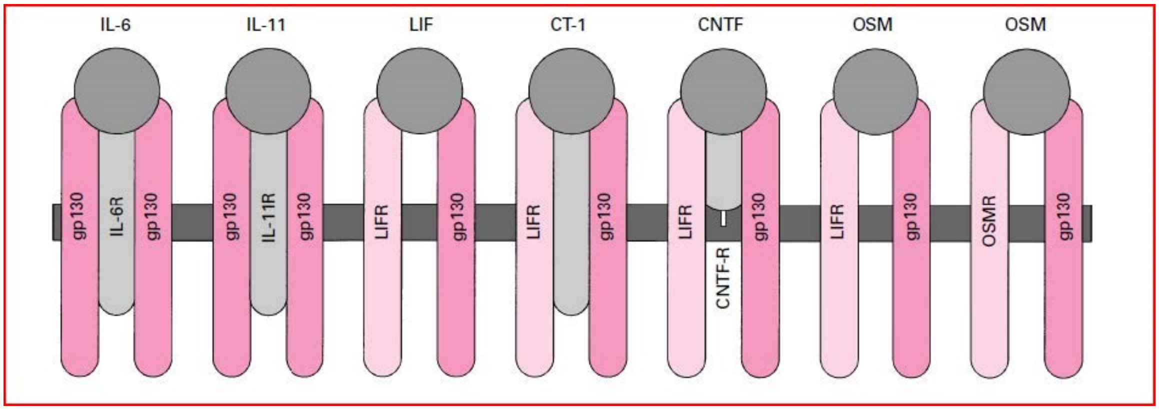

Figure 1: Common membrane receptors for IL-6 family of cytokines.

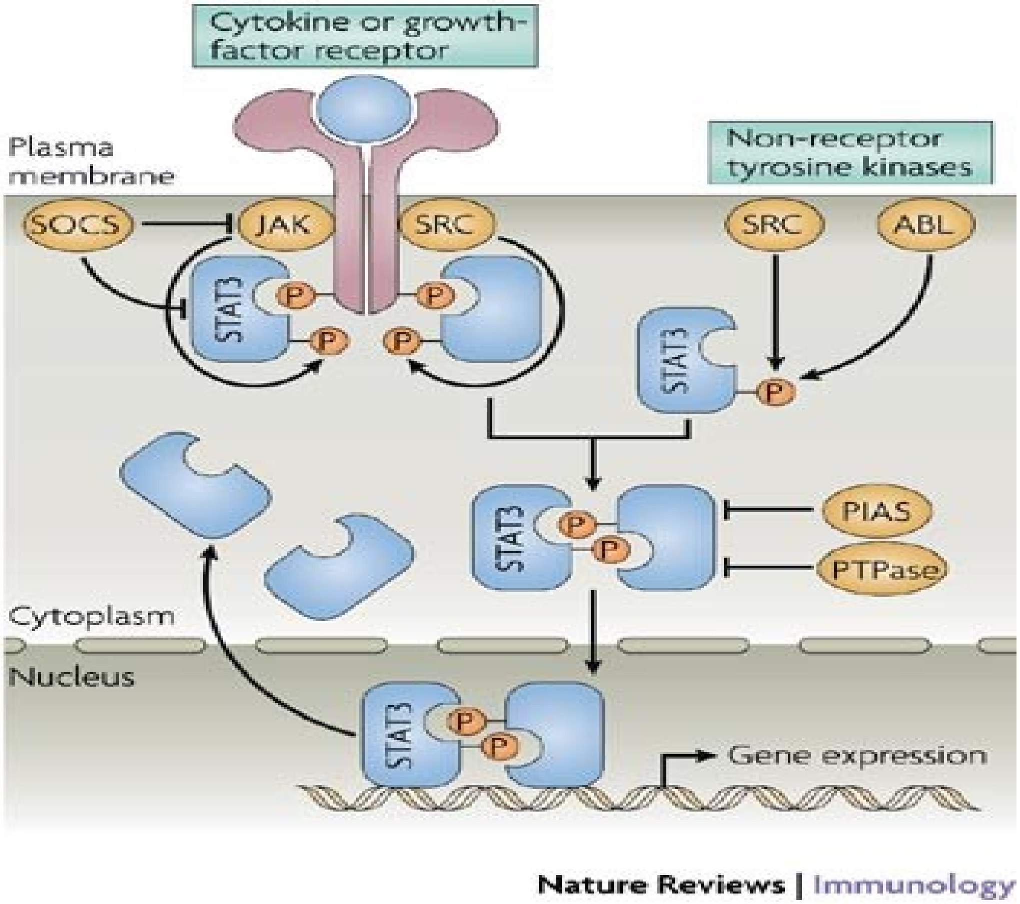

Figure 2: The JAK-STAT signaling pathway. (Figure is adapted from Yu H, Kortylewaski M, Pardoll D. Crosstalk between cancer and immune cells: role of STAT3 in the tumor microenvironment. (Nature Reviews Immunology. 2007; 7:41-51.)

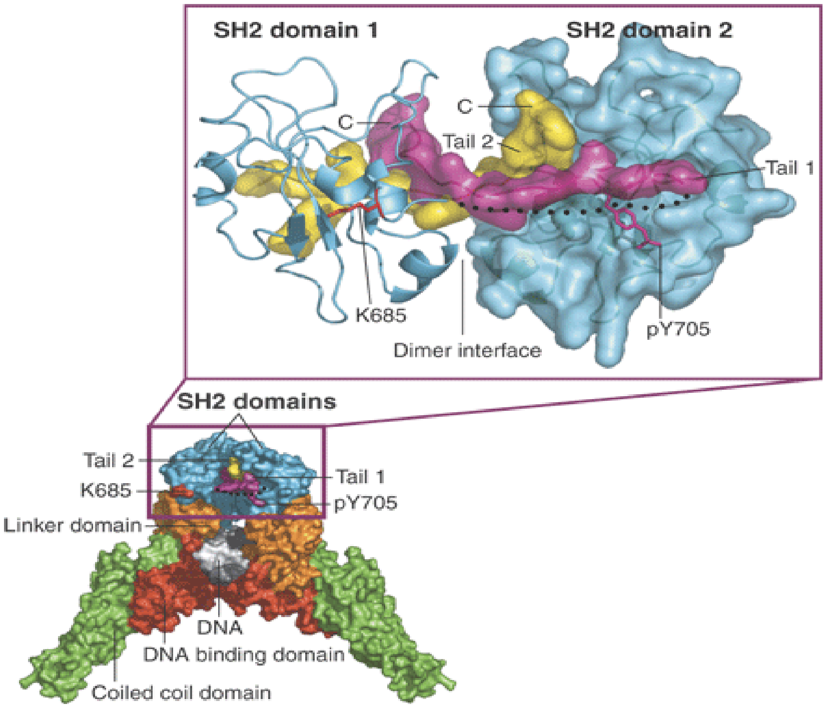

Figure 3: Three-dimensional structure of activated STAT3 protein dimer. (Figure is adapted from O'Shea JJ, Kanno Y, Chen Y, Levy DE. (Cell Signaling. Stat acetylation--a key facet of cytokine signaling? *Science*. 2005;307:217-218.)

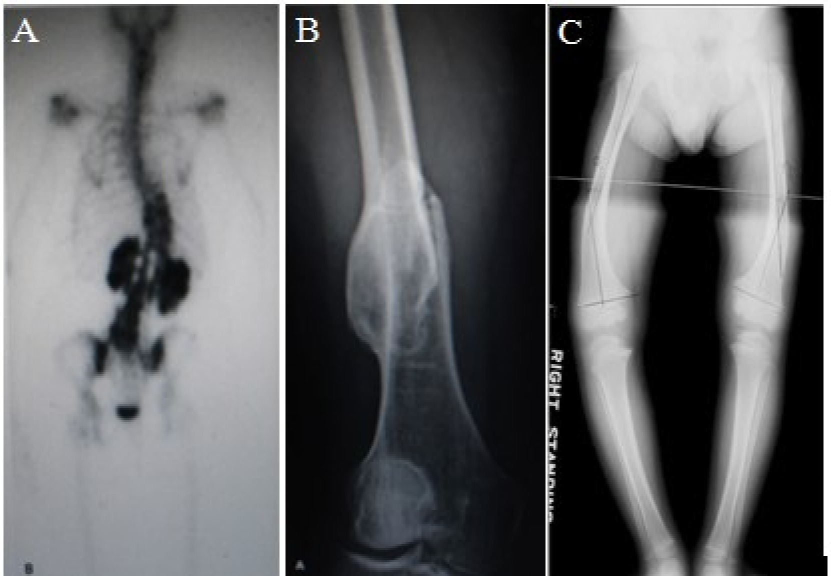

Figure 4: The observed bone phenotypes in HIES patients. A: X-ray image of spinal scoliosis; B: pathological fracture in distal femur of HIES patient in the process of healing; C: Bowing of the legs of a 3-year-old HIES patient

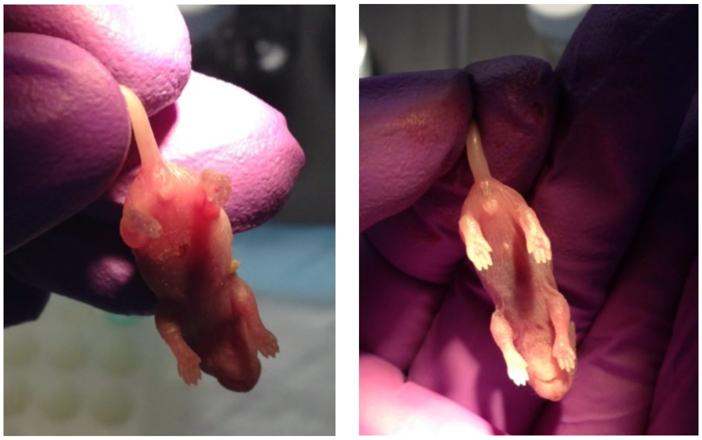

Figure 5: Visual determination of the sex of newborn pups based on the presence or absence of scrotal pigmentation; female (left) and males (right).

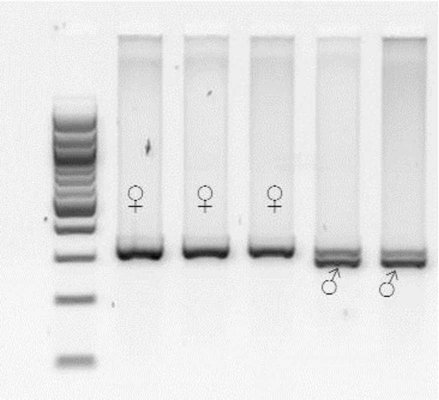

Figure 6: Genotyping of the sex genes for diaphonized pups. Females amplify one band while males amplify two bands.

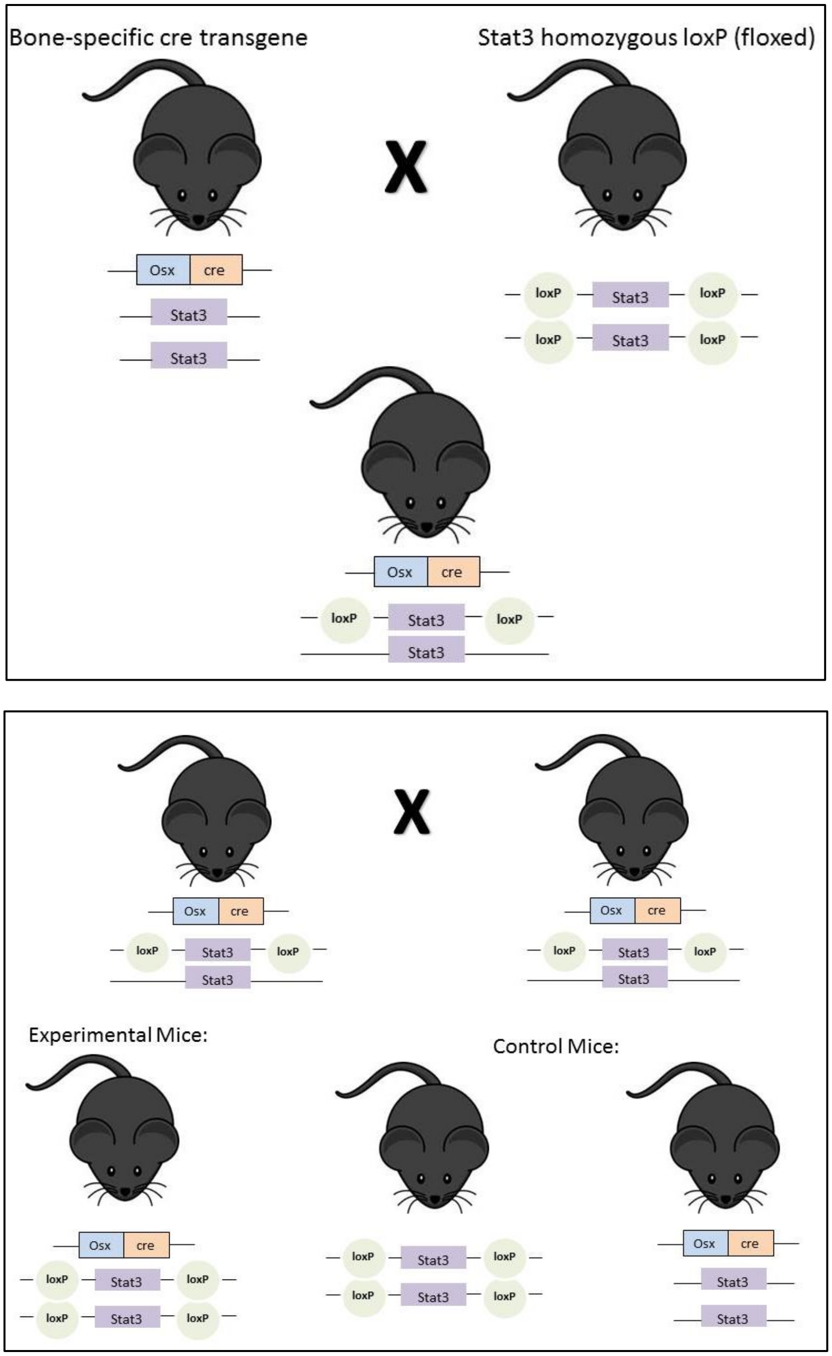

Figure 7: Breeding scheme for pre-osteoblast specific STAT3 mice.

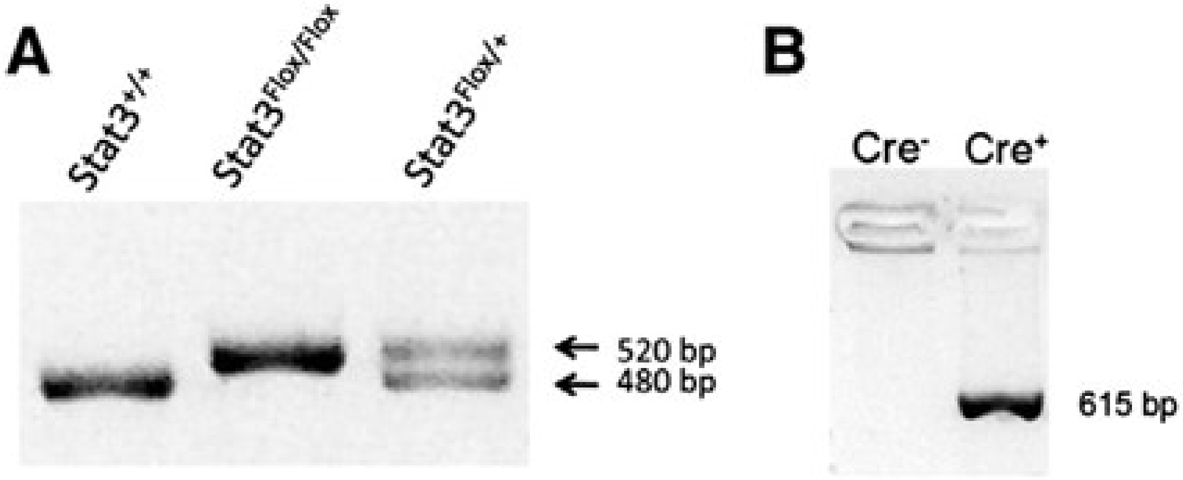

Figure 8: PCR amplification and identification of Cre and STAT3 genes. The smaller 490bp belongs to the STAT3 $^{(+/+)}$ (wild type) mice while the 520bp fragments contain loxp sites and belongs to the cKO mice. The 615 bp band represents the presence Cre.

a)

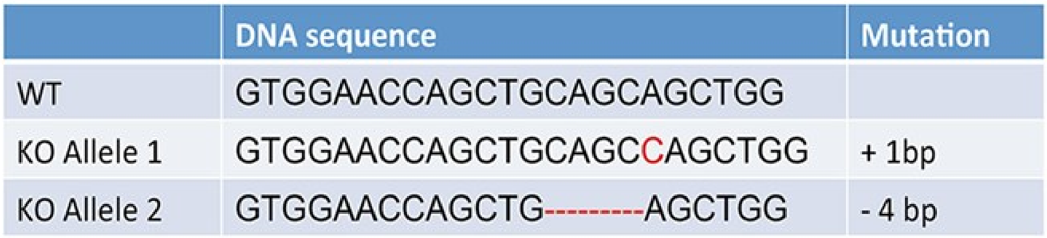

	DNA sequence	Mutation
WT	GTGGAACCAGCTGCAGCAGCTGG	
KO Allele 1	GTGGAACCAGCTGCAGCCAGCTGG	+ 1bp
KO Allele 2	GTGGAACCAGCTG---------AGCTGG	- 4 bp

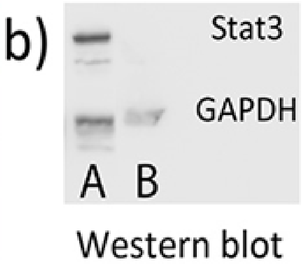

Figure 9: Generation and confirmation of STAT3 KO cell line. a. DNA sequencing of the WT and STAT3 KO immortalized cell lines shows that one KO allele has an extra base pair while the other KO allele has four missing alleles. b. Western blot analysis confirmed the successful deletion of *Stat3* expression from the KO cells

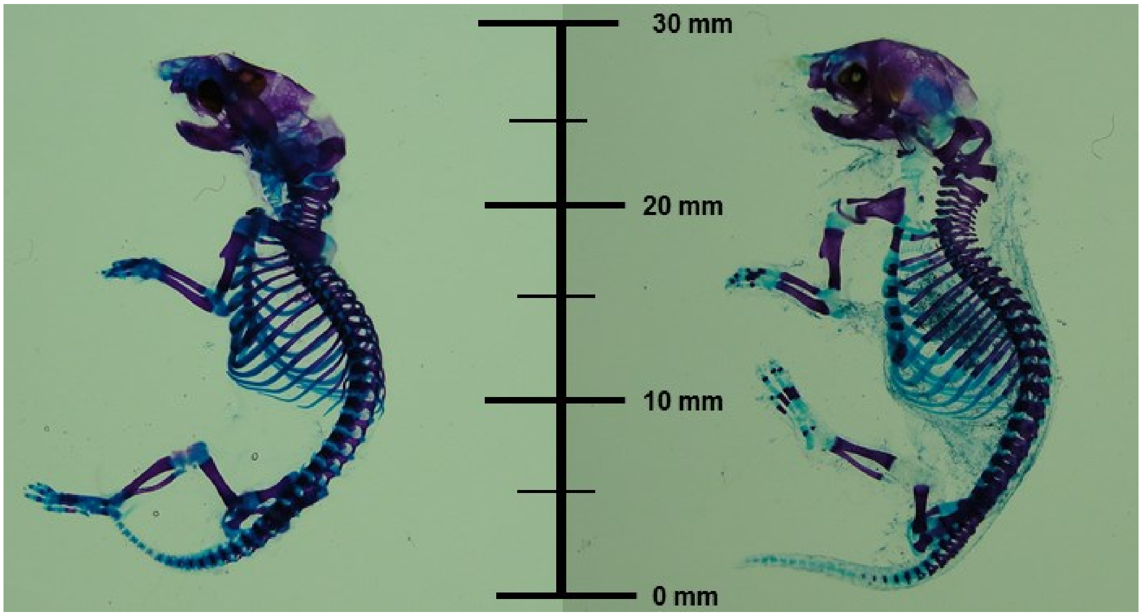

Figure 10: Whole skeletal preparations of newborn WT and cKO pups showed no significant differences in body size or mineralization.

Figure 11: Diaphonization of the newborn mice. Osx-cre STAT3 WT and cKO mice showed no significant differences in the area of mineralization and cartilage formation.

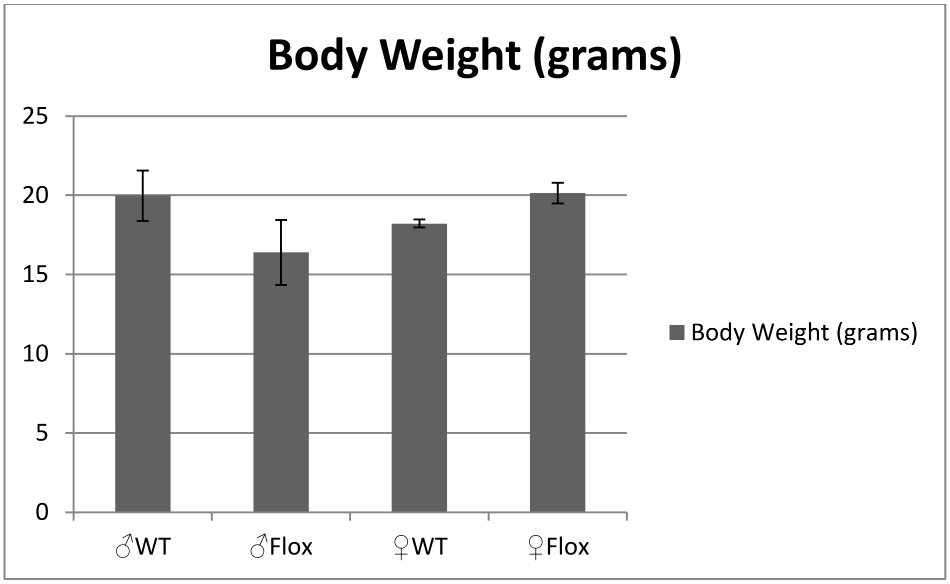

Figure 12: Body weights of experimental mice at 8 weeks of age. No significant differences were observed.

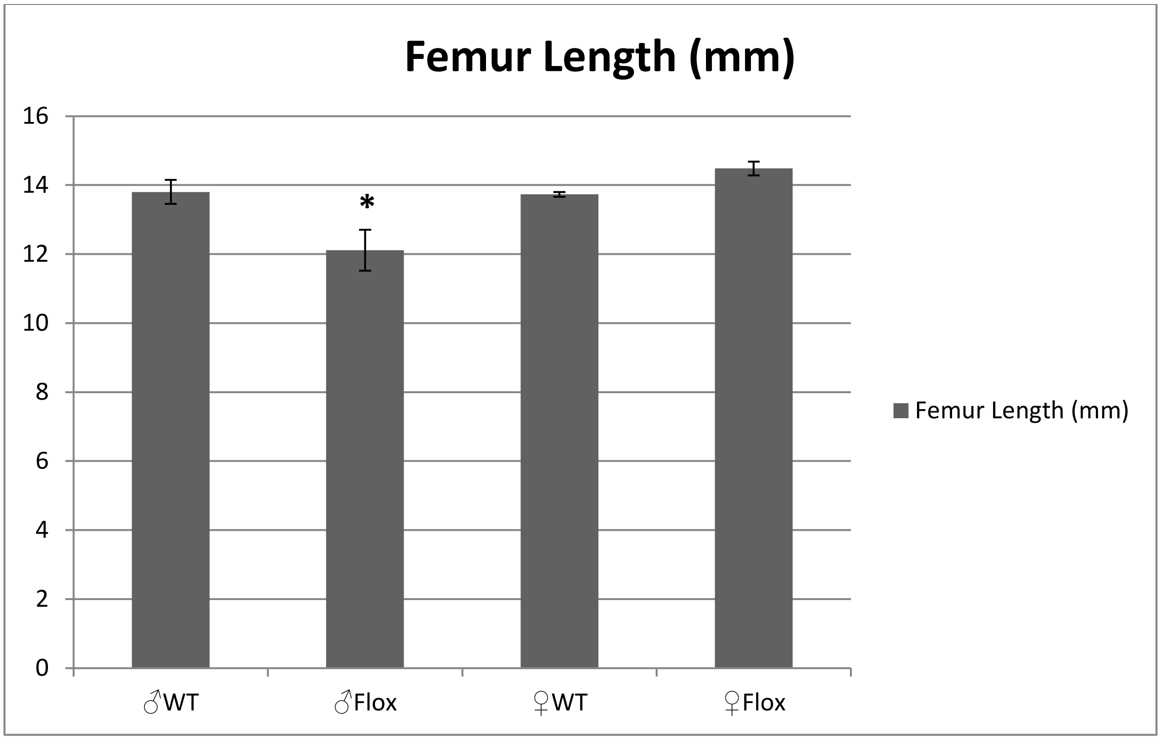

Figure 13: Femur lengths of 8 week old experimental mice. Male cKO mice had significantly shorter femurs than the WT controls.

Figure 14: Dissected femurs of male experimental mice. Conditional STAT3 males presented with significantly shorter femurs and had widened out cortical bone distal to the growth plate.

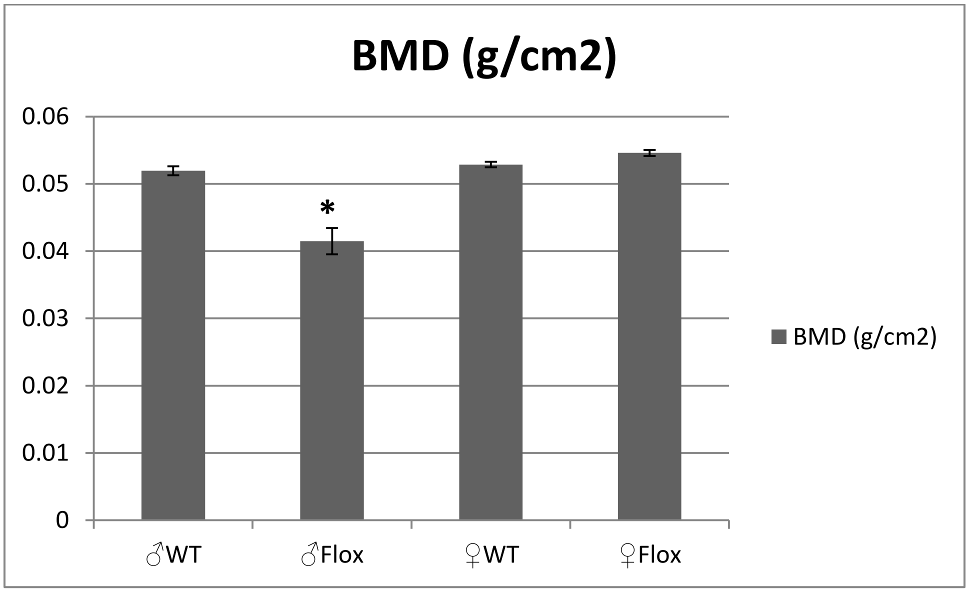

Figure 15: BMD of experimental mice. PIXImus scans of the femurs reveal differences in the BMD. Male cKO mice had significantly reduced BMD as compared to the WT controls.

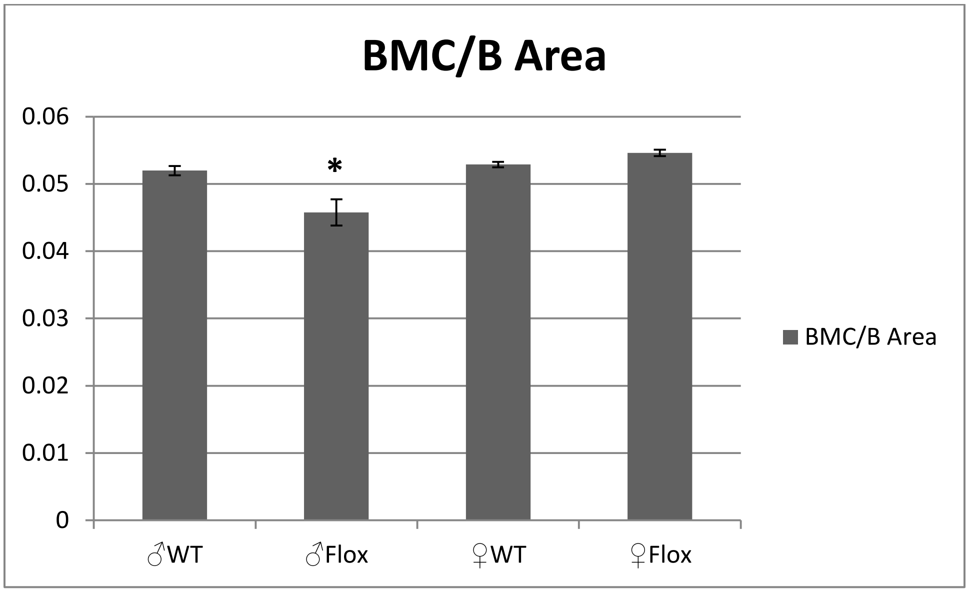

Figure 16: BMC of experimental mice. PIXImus scans of the femurs reveal differences in the BMC/B.Area. Male cKO mice had significantly reduced BMC/B.Area as compared to the WT controls.

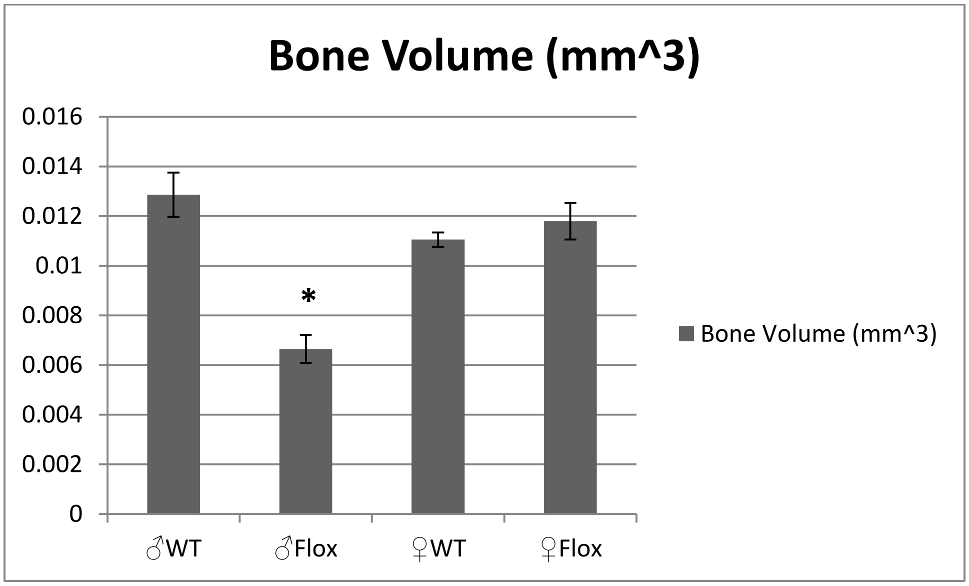

Figure 17: BV cortical bone analysis in the proximal third of the femur near the widened portion. Male cKO mice had significantly reduced bone volume in this region.

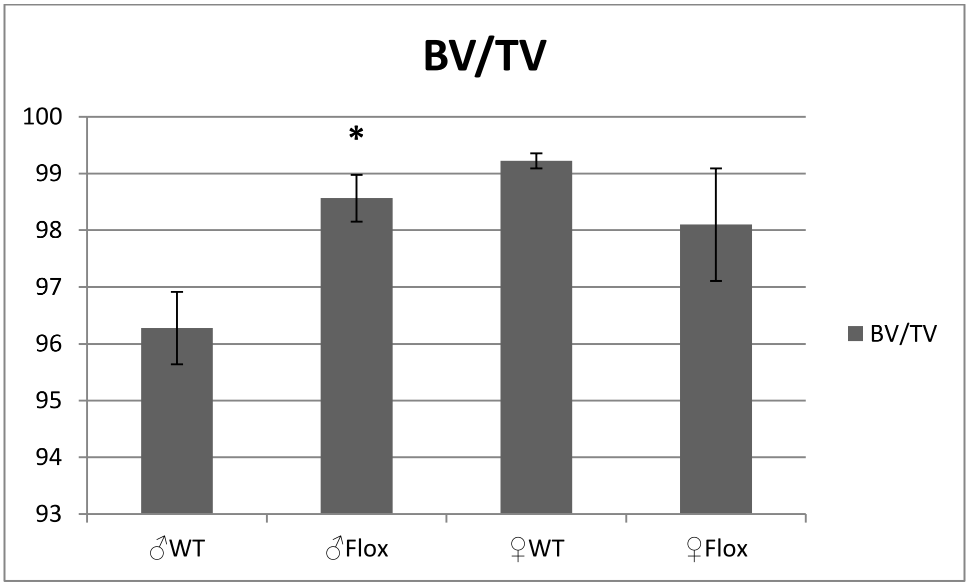

Figure 18: BV/TV cortical bone analysis in the proximal third of the femur near the widened portion. Male cKO mice had significantly more BV/TV in this region.

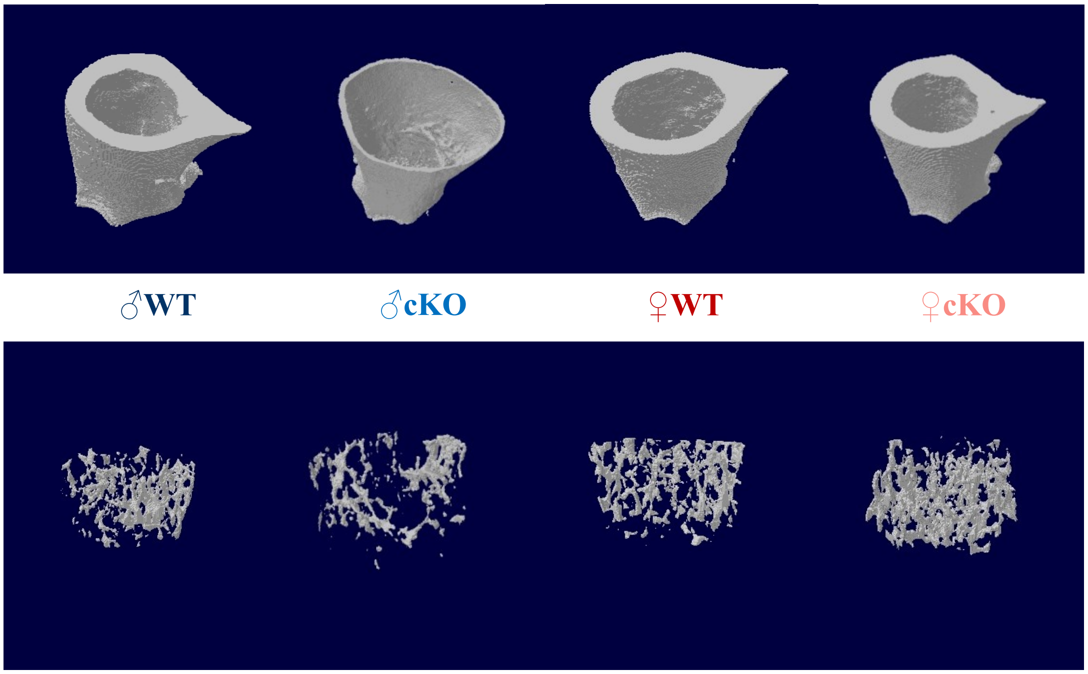

Figure 19: Three dimensional models comparing the proximal femurs of the experimental mice. Male cKO mice presented with severe widening and thinning of the cortical bone in this region.

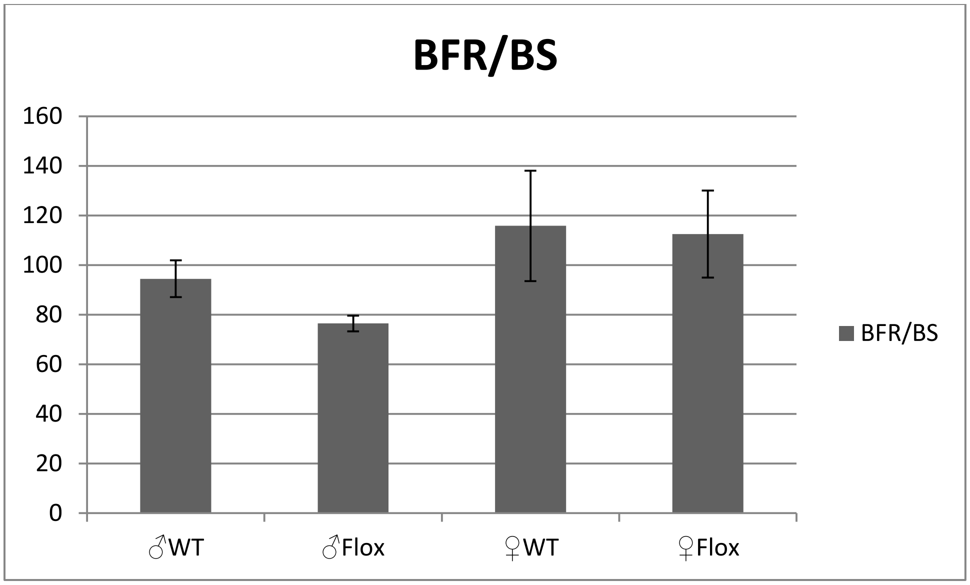

Figure 20: Analysis of the fluorochrome labels in the distal trabecular region revealed no significant differences.

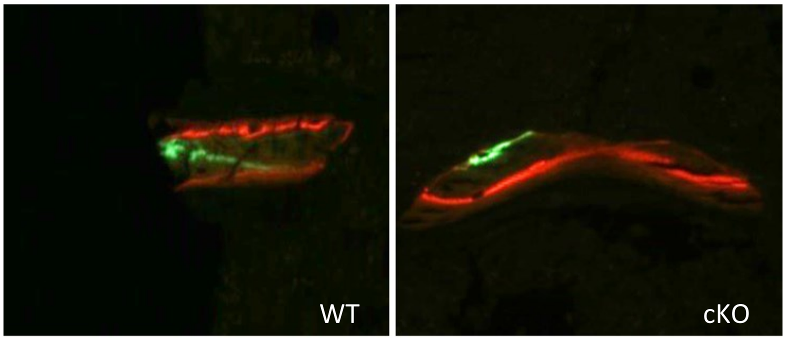

Figure 21: Distal femur fluorochrome labeling. No significant differences were observed

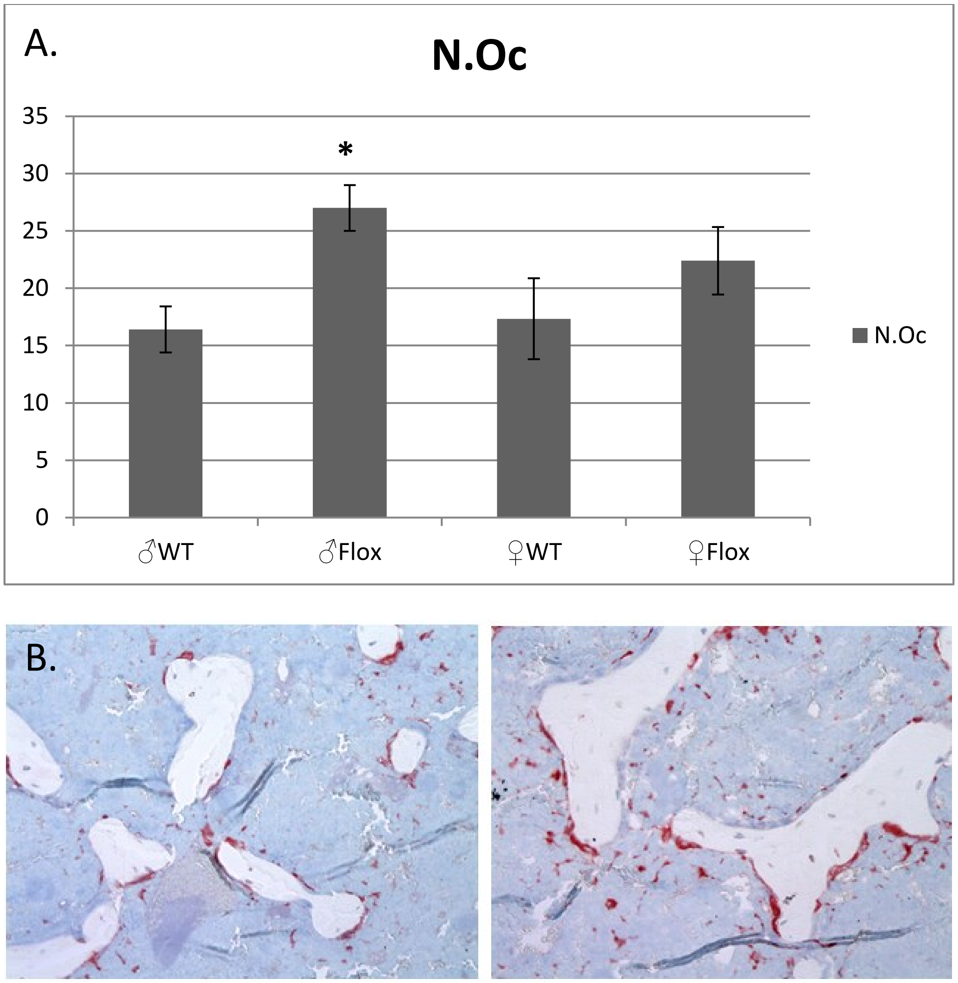

Figure 22: A. Analysis of TRAP stained sections in the distal trabecular region of the femurs showed that the male KO had significantly greater number of osteoclasts on the bone surfaces. B. 200x magnification showing the increased number of osteoclasts on surface of the KO mice (right).

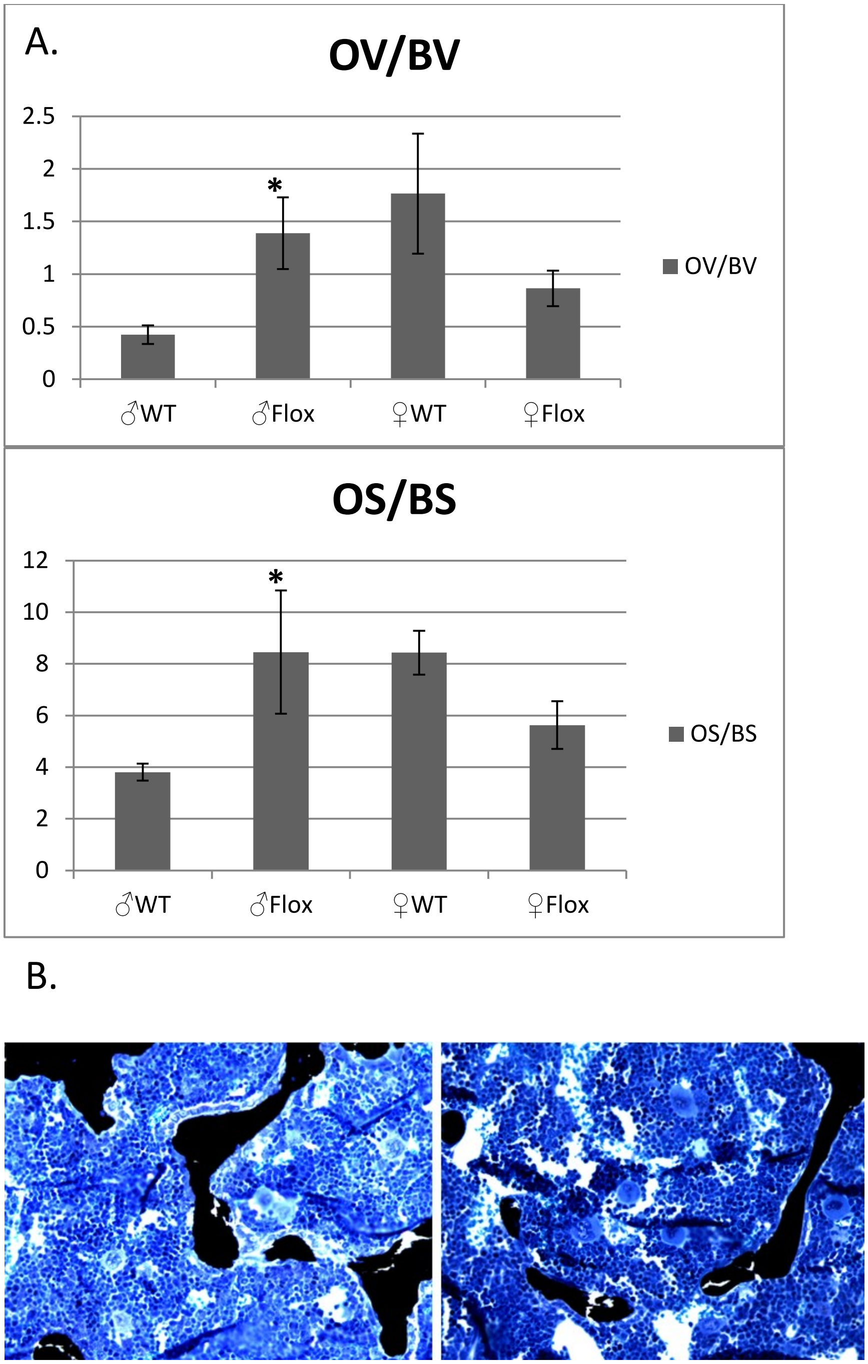

Figure 23: A. Analysis of the VKM slides in the distal trabecular region revealed that the male cKO mice had more OV/BV and increased OS/BS.

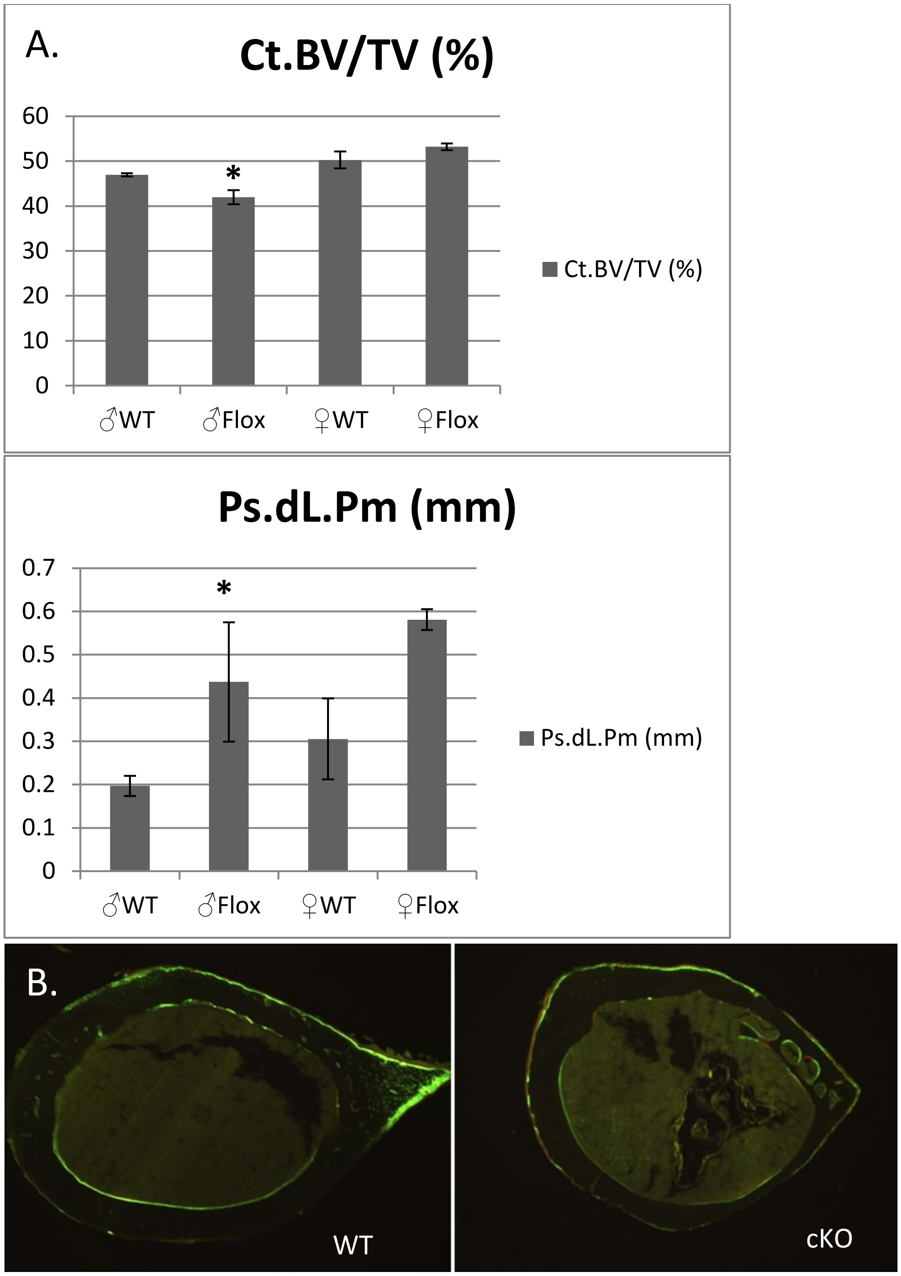

Figure 24: A. Analysis of the fluorescent labels in the femoral midshaft region of the femurs of the 8-week-old experimental mice revealed differences in Ct. BV/TV and Ps.dL.Pm. Male cKO mice had reduced BV/TV of the cortical bone yet increased double labeling on the periosteal surface. B. 200x magnification image of the fluorescent labels.

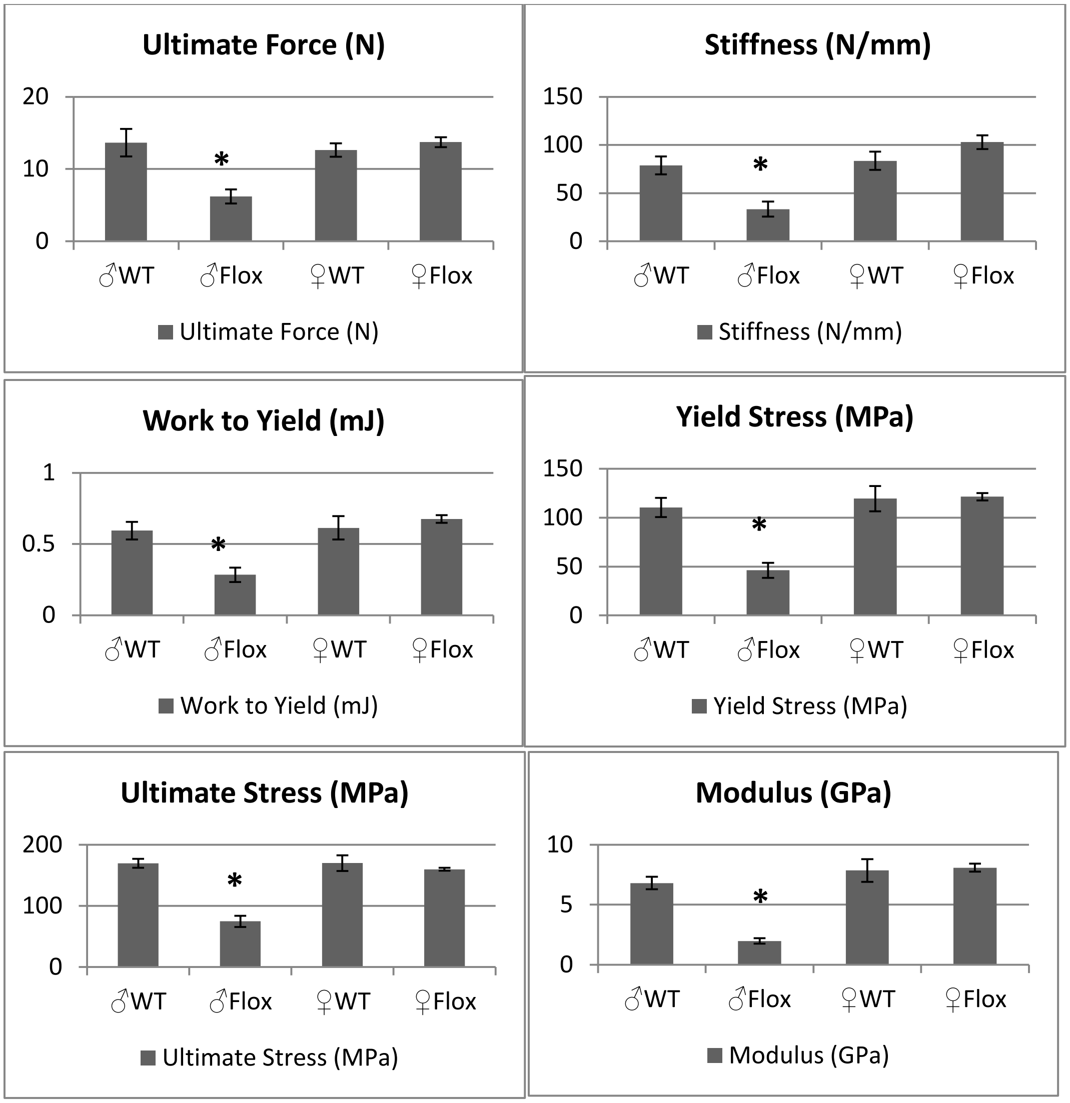

Figure 25: Results from biomechanical testing. Mechanical testing utilizing 3 point bending techniques showed significant differences in multiple parameters, including ultimate force, stiffness, work to yield, yield stress, ultimate stress, and Young’s modulus.

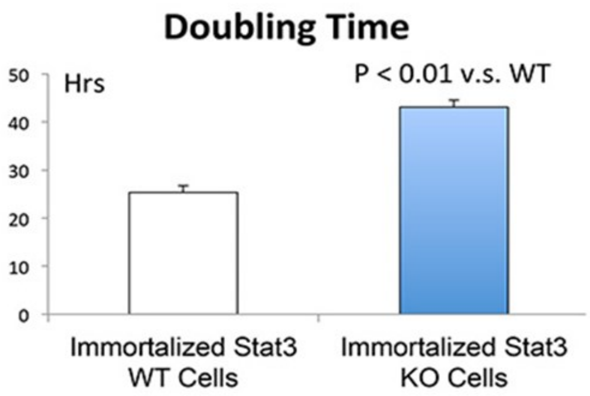

Figure 26: Doubling time experiment with STAT3 WT and KO cells. KO cell showed significantly greater doubling time as compared to the WT control cells.

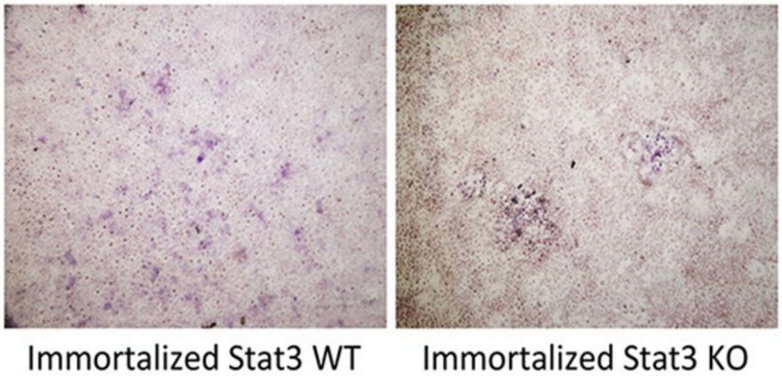

Figure 27: ALP staining of STAT3 WT and KO cells. STAT3 KO cells showed less ALP staining as compared to the WT control cells.

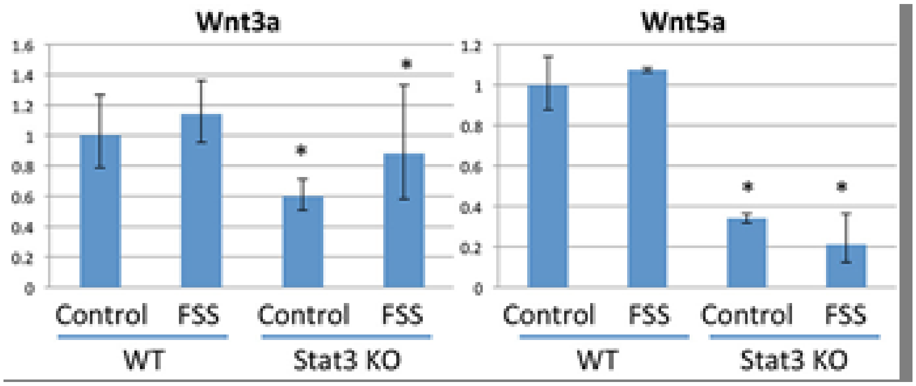

Figure 28: RT-qPCR analysis of STAT3 WT and KO cell lines. KO cells had significantly less mRNA levels of both Wnt3a and Wnt5a.

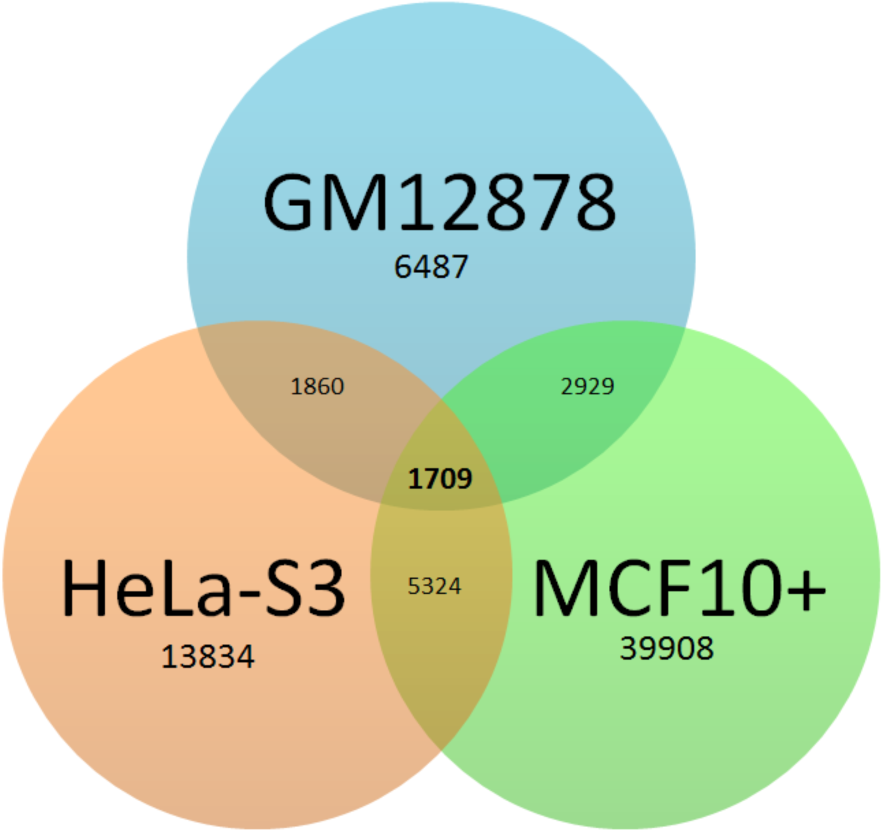

Figure 29: Venn diagram showing the overlap of STAT3 binding sites from the three different cell lines found in the ENCODE database.

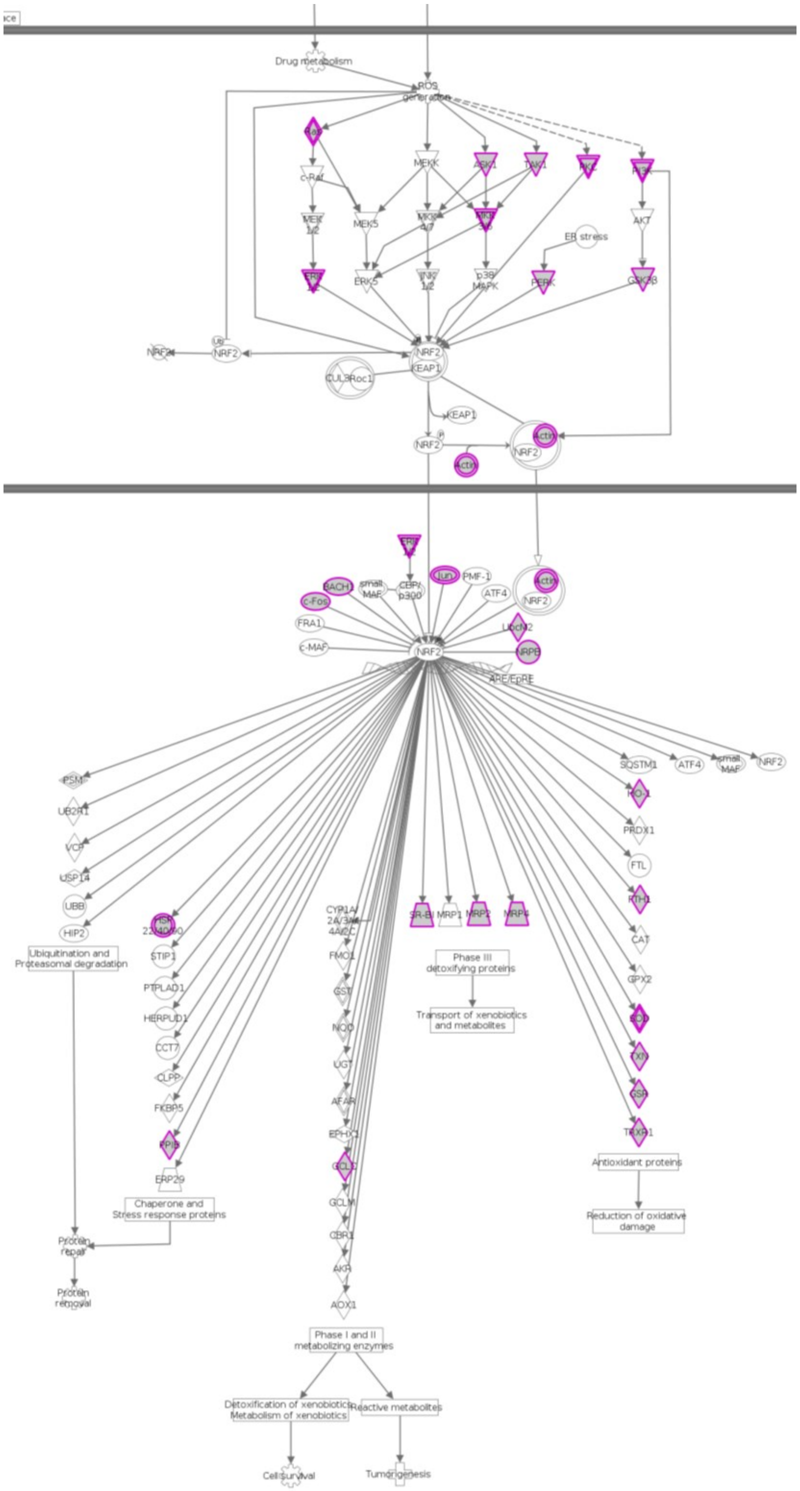

Figure 30: IPA schematic depicting Nrf2-signaling pathway. Bioinformatic profiling using Ingenuity Pathway Analysis showed that STAT3 was bound to a significant number of genes involved in Nrf2-signaling.

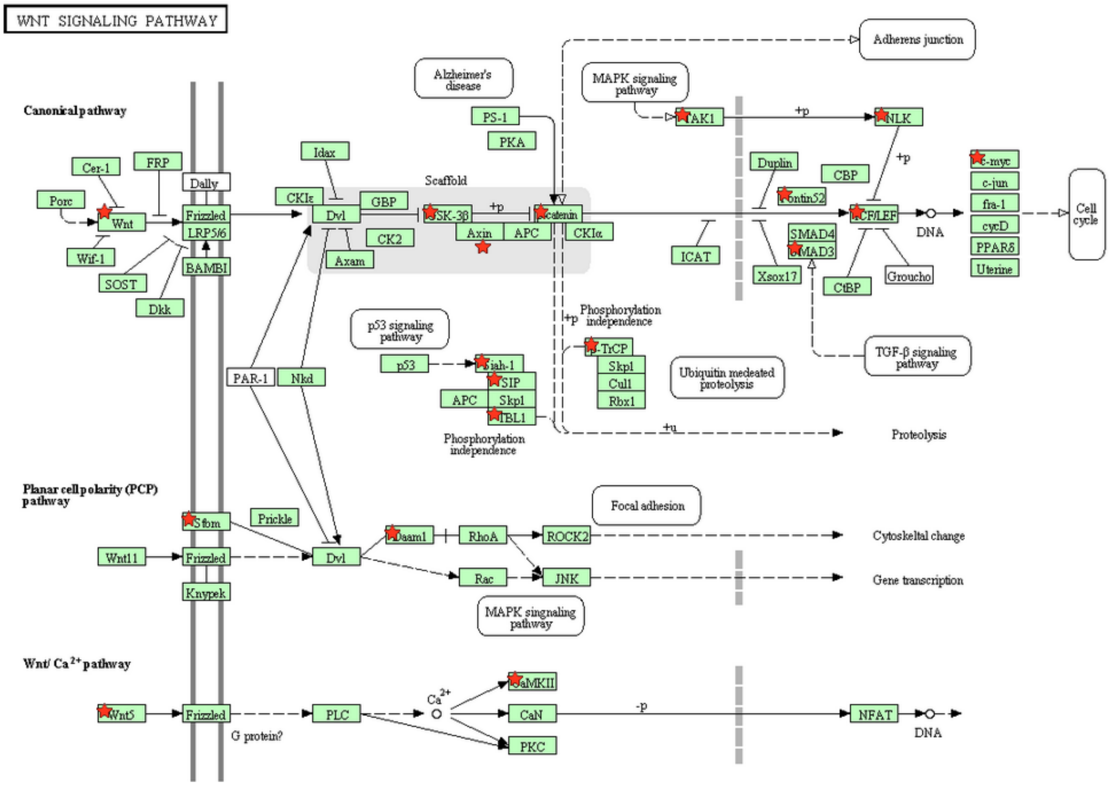

Figure 31: DAVID/KEGG schematic depicting Wnt-signaling pathway. Bioinformatic profiling using DAVID/KEGG showed that STAT3 was bound to a significant number of genes involved in the Wnt signaling pathway (shown by red stars). .